

Fabrication of $\text{Gd}_5(\text{Si}_{1-x}\text{Ge}_x)_4$ nanoparticles by femto and nanosecond pulsed laser ablation in liquids

David José Pereira Coelho

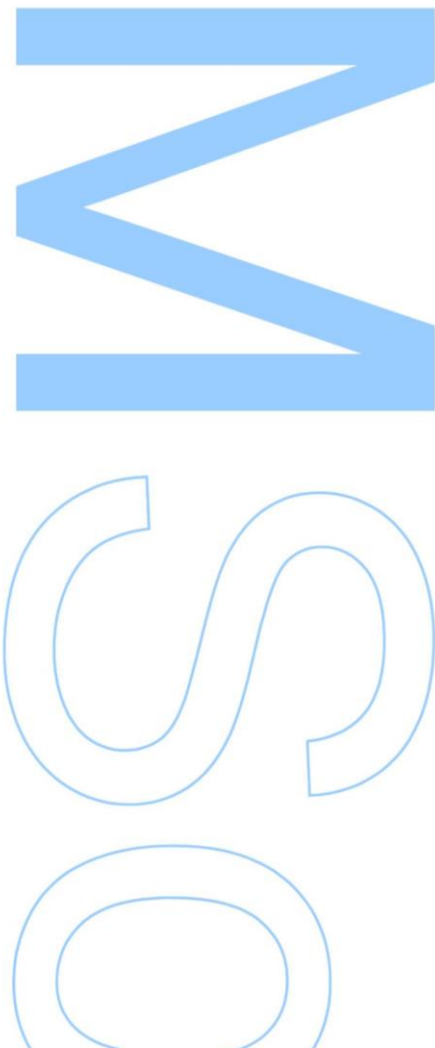
Mestrado Integrado em Engenharia Física
Departamento de Física e Astronomia
2017/2018

Orientador

Prof. João Pedro Esteves de Araújo, FCUP

Co-orientador

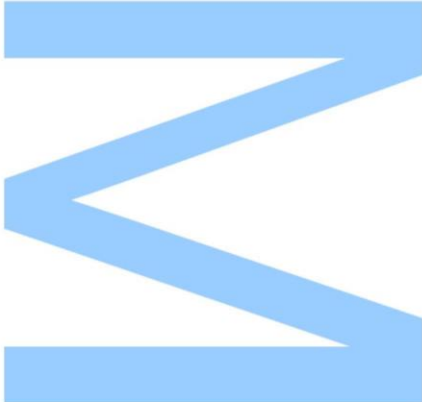
Prof. André Miguel Trindade Pereira, FCUP



Todas as correções
determinadas pelo júri, e só
essas, foram efetuadas

O presidente do Júri,

Porto, ____/____/____



“It is better to live one day as a lion than a hundred years as a sheep”

Italian Proverb

Acknowledgements

I could not have done this work all by myself. This includes help and support from my colleagues at Faculty of Sciences of the University of Porto, as well as support from my friends and family. In that way, I want to express my gratitude to all of those people.

To start, I want to thank to Professor João Pedro, for inviting me to this project, and for guiding me during the duration of the work. Thank you for all the help, support and for cheering me up when things seemed most hard to achieve. I hope that, if possible, I can continue working you in the future.

To professor André Pereira to all the advices and support that it has provided throughout the work.

To Vivian Andrade, whose help was invaluable during all of the work. Thank you for helping me achieve what I have accomplished, the constant support and motivation to go on, and also for the (positive) pressure you have put on me to never let me give up.

To João Horta, for the initial aid and advices, and also for the opportunity of following his work in magnetic materials in IFIMUP.

To professors Hélder Crespo and Bernardo Silva, responsible for the Femtosecond and Nanosecond lasers, respectively, that were used in this work. It was a pleasure to work with both, and I want to thank all the help provided from you. Also, I would like to mention the help of Miguel Noronha Canhota for the assistance in the Femtolab and for providing the understanding of the optics related topics.

I would also like to thank my colleagues, for sharing some of their knowledge and experience, for their support, and for the coffee breaks during those days of hard work.

To my family, for believing in me and for helping me get to the end of the degree, always supporting me. Also, to my friends outside the academic world, for all the cheering, and for helping me forget all of my problems. I will never forget your help.

Abstract

Rare earths compounds are among the most promising materials in the magnetic materials field. Due to their large magnetic properties, these materials are desirable for the implementation on many applications (hard disks, refrigeration, biological, materials coatings, etc.). The main goal of this work was to obtain magnetic nanoparticles through laser ablation of the target material in liquid media, and to characterize these particles (crystalline and magnetic structures, morphology, magnetization, ...). Ablation in liquid media is more recent than the usual ablation in vacuum or under inert or reactive atmosphere, presenting new characteristics and properties of the fabricated nanoparticles. Such goal was achieved by the implementation of a setup that is able to perform the expected ablation using nanosecond or femtosecond lasers, allowing to compare the nanoparticles obtained with both methods. The results obtained show that Laser ablation in liquids is a very promising method to prepare nanoparticles of $Gd_5(Si_{1-x}Ge_x)_4$ to be used in different applications ranging from biomedicine to magnetostrictive sensors.

Keywords

Laser ablation, liquid medium, $Gd_5(Si_{1-x}Ge_x)_4$, nanoparticles

Resumo

Compostos de terras raras são atualmente dos materiais mais promissores na área dos materiais magnéticos. Devido às suas propriedades magnéticas, estes materiais são desejáveis para a implementação em muitas aplicações (discos duros, refrigeração, biológicas, revestimento de superfícies, etc.). O objetivo principal deste trabalho foi obter nanopartículas magnéticas através de ablação a laser do material alvo em meio líquido, e caracterizar estas partículas (estruturas cristalinas e magnéticas, morfologia, magnetização, ...). Ablação em meios líquidos é mais recente do que a habitual ablação em atmosfera gasosa ou em vácuo, conferindo novas características e propriedades às partículas fabricadas. Tais objetivos foram alcançados, ao implementar uma montagem experimental capaz de efetuar a ablação esperada tanto com laser de nano quanto com laser de femtosegundo, permitindo assim uma comparação entre as nanopartículas obtidas. Os resultados obtidos pelos dois métodos mostram que ablação laser em líquidos é um método promissor para o fabrico de nanopartículas de $Gd_5(Si_{1-x}Ge_x)_4$ para serem usadas em aplicações que vão desde biomedicina a sensores magnetoestrictivos.

Palavras-chave

Ablação a laser, meios líquidos, $Gd_5(Si_{1-x}Ge_x)_4$, nanopartículas

Index

Aknowledgements	i
Abstract.....	ii
Resumo.....	iii
Index.....	iv
List of figures.....	vi
List of tables.....	xi
List of abbreviations.....	xii
Chapter 1 – Short Introduction and contents	1
Chapter 2 - The pathway for micro/nanostructuring of the $Gd_5(Si_{1-x}Ge_x)_4$ family compounds	3
2.1 - $Gd_5(Si_{1-x}Ge_x)_4$ family of materials.....	3
2.1.1 - Structural and magnetic phases.....	3
2.1.2 - Phase transition and magneto structural coupling of $Gd_5(Si_xGe_{1-x})_4$	5
2.2 - Laser interactions with matter.....	7
2.2.1 - Ablation mechanisms.....	7
2.2.2 - Femtosecond laser ablation of dispersed powders in solution (FLAS)	14
2.2.3 - Experimental parameters.....	15
2.2.4 - Liquid confinement, thermodynamic and kinetic properties.....	17
2.2.5 - Nanocrystal formation.....	22
2.2.6 - Comparison between Femtosecond and Nanosecond laser ablation	24
2.2.7 - Liquid confinement, thermodynamic and kinetic properties.....	31
Chapter 3 – Experimental techniques.....	33
3.1 – Setup.....	33
3.1.1 - Nanosecond KrF Excimer PLAL setup.....	33

3.1.2 - Femtosecond Ti:Sapphire PLAL setup.....	34
3.2 – Experimental techniques.....	34
3.2.1 - Scanning electron microscopy (SEM).....	35
3.2.1.1 - Scanning Transmission Electron Microscopy (STEM).....	37
3.2.1.2 - Energy Dispersive (X-Ray) Spectroscopy (ED(X)S).....	38
3.2.2 - X-Ray Diffraction (XRD).....	40
3.2.3 – Vibrating Sample Magnetometer.....	42
3.3 – Experimental Procedure.....	44
Chapter 4 – Results and discussion.....	45
4.1 - Targets structural and chemical characterization.....	45
4.2 - $Gd_5(Si_xGe_{1-x})_4$ and Ni nanoparticles.....	49
4.2.1 - Morphological and chemical characterization.....	49
Chapter 5 – Conclusion and Future Work.....	61
Bibliography.....	63

List of figures

Figure 1 - (a) and (b) Illustration of the constituting blocks of the slabs of the $R_5(Si_{1-x}Ge_x)_4$ family. (c) is the perspective from the a-b plane, which represents a slab. (d) is the perspective of the a-c plane, showing the connection of adjacent slabs in the b direction [4]..... 4

Figure 2 - (a) Possible structures of the $R_5(Si_{1-x}Ge_x)_4$, where the difference from each other is based on the number of T1-T1 interslab bonds existent. (b) a structural and magnetic phase-diagram of $Gd_5(Si_xGe_{1-x})_4$ for different temperatures and Si concentration is illustrated, delimiting the regions of different structural and magnetic phases [2], [4]..... 5

Figure 3 - Free energy as a function of temperature for both the (M) and O(I) structures, for the case of (a) $Gd_5Si_2Ge_2$ and (b) $Tb_5Si_2Ge_2$ [6]. 6

Figure 4 - (A) Schematic temperature (T)-density (ρ) phase diagram and typical FLAS paths (b→b1, c→c1, d→d1 and e→e1). (B) Possible mechanisms as a function of fluence. I: Spallative ablation; II: Phase explosion ablation, III: Spinodal decomposition, IV: fragmentation and vaporization, V: Plasma ablation and Coulomb explosion. α : ablation threshold. β : optical breakdown threshold (plasma formation threshold) (after [14]) 8

Figure 5 - Spallation process [15]. The times in the image are characteristic times, used in the model of the author (D. Perez). Note: this image is used only for descriptive purposes. After characteristic times defined by the author, it can be seen the complete removal of a layer of material from the target surface. From the image on the left it is possible to see the voids created, and as time progresses, these voids will increase until the ejection of the layer..... 9

Figure 6 - Time-resolved reflectivity images of silicon (upper row) and germanium (lower row) at different delay times. The laser parameters are $\lambda_{pump} = 400$ nm, 120 fs pulse, $1.4 \text{ J}\cdot\text{cm}^{-2}$. Frame size is $126 \times 95 \mu\text{m}^2$ (after [17])..... 10

Figure 7 - (A) Snapshots of the ablated area, and (B) Temperature spatial distribution for different time steps (image presented in [14], which was in turn adapted and with permission from [19]) 11

Figure 8 - A scheme of FLA and a SEM image of an ablated area. From the image, one can see that non-thermal processes are present due to the lack of molten material [23]. Laser parameters are 200 fs, 120 μJ , $F = 0.5 \text{ J}\cdot\text{cm}^{-2}$ with wavelength of 780 nm. Hole thickness is 100 μm 12

Figure 9 - (A) Images taken from a CCD camera of the plasma plume induced by femtosecond laser irradiation of a Titanium target. The images are recorded at various delay time after the femtosecond laser pulse for different camera gates depending on the intensity of the signal. (B) Shock wave propagation 4 ns after the ablation pulse with a probe wavelength of 400 nm and (C) 90 ns after the ablation pulse with a probe wavelength of 525 nm (image included in [14], which in turn was adapted with permission from [25], [26]) 13

Figure 10 - Craters in the surface of a gold target after 5000 pulses at (a) $F = 60 \text{ J}\cdot\text{cm}^{-2}$ and (b) $F = 1000 \text{ J}\cdot\text{cm}^{-2}$ [27]..... 14

Figure 11 – Mechanisms of FLAS of dispersed powders in solution. In sequence, from top to bottom: photothermal ablation by multiphoton absorption and consequent heating, resulting in melting; Electronic emission, creating the charge repulsion that originates Coulomb explosion; Near field enhancement (after [14])..... 15

Figure 12 – 4 steps of plasma plume evolution in PLAL: (a) creation of the plume due to the incidence of the laser energy; (b) expansion of the plume ; (c) chemical reactions between target material and surrounding liquid, during the plume expansion; and (d) plasma plume condensation, either floating to surface (smaller nanoparticles) or condensation in the bottom of the liquid (larger nanoparticles) (after [7]) 18

Figure 13 - Image of plasma plume light emitting region and respective intensity distribution from the ablation of a graphite target in water, using a Nd:YAG laser with wavelength of 1064 nm, a pulse duration of 20 ns, and fluence of $10 \text{ J}\cdot\text{cm}^{-2}$ (as exposed in [7] and its references) 19

Figure 14 - Illustration of the recording of an acoustic wave generated in water and the shock wave in the target, to measure the pressure generated at the plume (after [7])..... 20

Figure 15 – Si laser ablation rate depending on water layer thickness, for a laser fluence of $3.1 \text{ J}\cdot\text{cm}^{-2}$ (after [44]) 21

Figure 16 – First peak-to-peak amplitude of the recorded acoustic wave, depending on water layer thickness, for a fluence of $3.1 \text{ J}\cdot\text{cm}^{-2}$ (after [44]) 21

Figure 17 - (a) Critical radius r^* and (b) Gibbs free energy $\Delta G(r^*)$ of diamond critical nuclei dependence on the temperature for various values of pressure (as exposed in [7]) 23

Figure 18 - Nucleation time dependence on pressure at given temperatures, for a graphite target to phase change to diamond. It is also possible to see the pressure-temperature diagram of carbon in inset [48] 24

Figure 19 – Timescales for both nanosecond and femtosecond pulsed laser ablation and visible emission from the plasma [49]. Optical emission occurs after the ablation process in both cases, but in femtosecond case, the ablation occurs well after the pulse ends, while in nanosecond ablation occurs while the pulse is still irradiating the target 25

Figure 20 – Illustration of timescales of nanosecond and femtosecond laser ablation processes, during and after the respective laser pulse [24]..... 26

Figure 21 - Free electron time dependence for the contributing processes, SEFI and EII. A 500 nm laser pulse, with an electric field of $150 \text{ MV}\cdot\text{cm}^{-1}$, with varying pulse lengths from 25 fs to 200 fs, irradiated on a SiO_2 target [52]..... 28

Figure 22 - Time and spectral integrated ICCD images of nanosecond and femtosecond laser-produced plasmas (LPP) under similar laser fluence conditions. The delay and integration times used for these images are 0 ns and 2 μs [49] 29

Figure 23 - Laser ablation craters in a 100 μm thick steel foil with (a) 200 fs, 780 nm and 120 μJ ; and (b) 3.3 ns, 780 nm and 1 mJ laser pulses (after [23], [24]) 30

Figure 24 – Ablated depth of a Si target in air and water environments, for a laser fluence of $4.5 \text{ J}\cdot\text{cm}^{-2}$. Clearly, a linear relation exists in both cases, with the ablation rate in liquid media being higher than in air [45]..... 32

Figure 25 - Nanosecond laser ablation setup. The purple line illustrates the optical beam path. The focal distance of the lens, before the mirror (beam splitter), is of 50 cm. 33

Figure 26 - Femtosecond laser ablation setup. The yellow line represents the beam optical path. The final lens focal distance is 100 mm..... 34

Figure 27 - Scanning Electron Microscopy (SEM) setup. The electron beam is accelerated in the anode, and then focused using magnetic lenses. The last path is through the scanning coils, where the beam is deflected horizontally and vertically, thus scanning the entire sample surface [58] 35

Figure 28 - Electron interaction along sample depth [59]..... 36

Figure 29 - STEM setup. As in SEM, the electron beam path is similar, with condenser lenses and deflection coils to scan the target. After the beam passes through the sample, is collected and then analyzed to form Annular dark-field (ADF) and Bright field (BF) imaging [61] 38

Figure 30 - SEM and EDX setup 39

Figure 31 - Illustration of Auger electrons and EDX spectroscopy principle [62]	39
Figure 32 - Bragg law, and X-Ray diffraction [64]	41
Figure 33 - Bragg-Brentano geometry [65]	41
Figure 34 - Parallel beam geometry [66]	42
Figure 35 – VSM setup scheme [67]	43
Figure 36 - Rietveld refinement of the XRD pattern of the $Gd_5Si_{2.2}Ge_{1.8}$ bulk target	45
Figure 37 – Rietveld refinement of the XRD pattern for the $Gd_5Si_2Ge_2$ bulk target.....	46
Figure 38 – $Gd_5Si_{2.2}Ge_{1.8}$ Magnetization dependence on temperature, for a fixed value of the magnetic field, for the cooling and heating curves	47
Figure 39 - $Gd_5Si_2Ge_2$ Magnetization dependence on temperature, for a fixed value of the magnetic field, for the cooling and heating curves.	47
Figure 40 - $Gd_5Si_{2.2}Ge_{1.8}$ magnetization dependence on magnetic field, for a fixed value of temperature of 5K.	48
Figure 41 - $Gd_5Si_2Ge_2$ magnetization dependence on magnetic field, for a fixed value of temperature of 5K.	48
Figure 42 - SEM images of the $Gd_5Si_{2.2}Ge_{1.8}$ sample, with laser parameters of 300 mJ energy per pulse and 1 Hz frequency rate, and ablation time of 20 minutes. (inset) Size distribution of analyzed nanoparticles, with average diameter of approximately 207 nm	49
Figure 43 - SEM images of the $Gd_5Si_2Ge_2$ sample, with laser parameters of 450 mJ energy per pulse and 10 Hz frequency rate, and ablation time of 2 hours and 20 minutes. (inset) Size distribution of analyzed nanoparticles, with average diameter of approximately 52 nm	50
Figure 44 - SEM images of the $Gd_5Si_2Ge_2$ sample, with laser parameters of 450 mJ energy per pulse and 10 Hz frequency rate, and ablation time of 4 hours. (inset) Size distribution of analyzed nanoparticles, with average diameter of approximately 32 nm	50
Figure 45 - (left) SEM image of the solution resultant of ablation of Nickel target for 5 minutes and (right) microscopic picture of the ablated area. There was not enough statistical data, so size distribution was not possible to obtain.....	52
Figure 46 – SEM images of the solution resultant of ablation of Nickel target for 10 minutes. (inset) Size distribution of the analyzed particles, with average particle size of 56,4 nm	53

Figure 47 – SEM images of the solution resultant of ablation of Nickel target for 30 minutes and collected at the bottom of the recipient. (inset) Size distribution of the analyzed particles, with average size particle of 165 nm 53

Figure 48 - SEM images of the solution resultant of ablation of Nickel target for 30 minutes and collected at the middle of the recipient. (inset) Size distribution of the analyzed particles, with average particle size of 23 nm 54

Figure 49 - SEM images of the solution resultant of ablation of Nickel target for 30 minutes and collected at the top of the recipient (near water surface). (inset) Size distribution of the analyzed particles, with average particle size of 34,5 nm 54

Figure 50 – Ni size dependence on time of ablation and depth of collected nanoparticles 55

Figure 51 - SEM images of the solution resultant of ablation of $Gd_5Si_2Ge_2$ target for 40 minutes and collected at the top of the recipient (near water surface). (inset) Size distribution of the analyzed particles, with average particle size of 65 nm 56

Figure 52 - SEM images of the solution resultant of ablation of $Gd_5Si_2Ge_2$ target for 3 hours and collected at the top of the recipient (near water surface). (inset) Size distribution of the analyzed particles, with average particle size of 57 nm 56

Figure 53 - SEM images of the solution resultant of ablation of $Gd_5Si_2Ge_2$ target for 4 hours. (inset) Size distribution of the analyzed particles, with average particle size of 56 nm 57

Figure 54 - SEM image of the solution resultant of ablation of $Gd_5Si_2Ge_2$ target for 8 hours. (inset) Size distribution of the analyzed particles, with average particle size of 57 nm 57

Figure 55 – Laser irradiation of (left) water solution and (right) $Gd_5Si_2Ge_2$ as prepared solution. The difference is clear, with more dispersion of the irradiating light in the as prepared solution. 58

Figure 56 – EDS analysis of the $Gd_5Si_2Ge_2$ sample, after 8 hours of ablation. 59

Figure 57 – Comparison between femtosecond and nanosecond on the average particle size depending on time of ablation. 59

Figure 58 – $Gd_5Si_2Ge_2$ Magnetization dependence on temperature, for a fixed value of the magnetic field, for the cooling and heating curves, for a low amount of sample collected. The resulting saturation magnetization is very low comparing to previous results 61

List of tables

Table 1 – Difference between nanosecond and femtosecond systems, considering the presented properties or aspects in the table. From an overall perspective, we can see that femtosecond systems present considerable advantages over nanosecond systems.....	31
Table 2 - Space group and refinement parameters of $Gd_5Si_2Ge_2$ and $Gd_5Si_2Ge_{1.8}$. Parameters a, b and c are unit cell lengths in nm.....	46

List of abbreviations

MCE - Magnetocaloric Effect

GMCE - Giant Magnetocaloric Effect

GMSE - Giant Magnetostrictive effect

CFC - Cloro Fluoro Carbons

IFIMUP - Instituto de Física dos Materiais da Universidade do Porto

CEMUP - Centro de Materiais da Universidade do Porto

CFUM - Centro de Física da Universidade de Braga

GMR - Giant Magnetoresistance

CMS - Colossal Magnetostriction

PM - Paramagnetic

FM - Ferromagnetic

AFM - Antiferromagnetic

$Gd_5(Si,Ge)_2$ - Gadolinium Silicium Germanium alloy

BCC - Body Centered Cubic

PLA - Pulsed Laser Ablation

PLAL - Pulsed Laser Ablation in Liquids

PLD - Pulsed Laser Deposition

FLAS - Femtosecond Laser Ablation in Solution

DLC - Diamond Like Carbon

SDS - Sodium Dodecyl Sulfate

PIP - Plasma Induced Plasma

LIP - Laser Induced Plasma

FWHM - Full Width Half Maximum

EII - Electron Impact Ionization

SEFI - Strong Electron Field Ionization

MPI - Multi Photon Ionization

TI - Tunnel Ionization

KrF - Krypton Fluor

Ti:Sa - Titanium Saphire

SEM - Scanning Electron Microscopy

TEM - Transmission Electron Microscopy

STEM - Scanning Transmission Electron Microscopy

BF - Bright Field

ADF - Annular Dark-Field

SE - Secondary Electrons

BSE - Back Scattered Electrons

ED(X)S - Energy Dispersive (X-Ray) Spectroscopy

XRD - X-Ray Diffraction

VSM - Vibrating Sample Magnetometer

Chapter 1 – Short Introduction and Contents

Over the last years, the rare-earth intermetallic $R_5(Si_{1-x}Ge_x)_4$ system has received much attention due to its magnetic and structural properties. These properties include the Magnetocaloric Effect (MCE), Giant Magnetostrictive Effect (GMSE), and others. These materials have the potential to revolutionize some applications on daily functions, like replacing CFC gases on refrigeration systems, introducing new medical treatments for killing cancer cells like magnetic hyperthermia, and many others. The main objective of this work was to develop a set-up to produce magnetic nanoparticles of the $R_5(Si_{1-x}Ge_x)_4$ systems and study their properties. This work is the first of a kind in the Institute of Physics of Materials of University of Porto (IFIMUP), particularly because this fabrication is achieved in liquid media combining the know-how of different groups of Universities of Minho and Porto.

After this short introduction, this thesis advances with the second chapter where the family of rare earth materials, particularly the $Gd_5(Si_{1-x}Ge_x)_4$ rare earth intermetallic compound are introduced, including their crystalline and magnetic structures, as well as the interplay between these structures. Also, the laser interaction with matter is discussed, including the mechanisms responsible for the fabrication of the desired nanoparticles.

The third chapter describes the experimental techniques and setups used and developed for the production of nanoparticles, as well as those used for the analysis and characterization of the produced systems.

The fourth chapter shows the obtained results, their analysis and discussion.

Finally, fifth chapter presents the conclusion of this work, possible future endeavors and goals.

Chapter 2 – The pathway for micro/nanostructuring of the $Gd_5(Si_{1-x}Ge_x)_4$ family of compounds

2.1 $Gd_5(Si_{1-x}Ge_x)_4$ family of compounds

The $R_5(Si_{1-x}Ge_x)_4$ family of compounds (R is for rare earth lanthanide element, like Gd, Tb, Dy, Ho, Er, etc.) has gained substantial interest due to its magnetic properties, more specifically to its application in magnetic refrigeration, after Gschneider and Pecharsky have found the Giant Magnetocaloric Effect (GMCE) in $Gd_5Si_2Ge_2$ at room temperature [1]. Other properties will only be mentioned, like unusual Hall effect, Giant Magnetoresistance (GMR) and Colossal Magnetostriction (CMS) [2]. This family of alloys are very sensitive to external parameters, like temperature, pressure and magnetic field, and internal parameters like stoichiometry and doping. In this subchapter, the crystallographic and magnetic structures will be presented, with special emphasis in the $Gd_5(Si_{1-x}Ge_x)_4$ case. Also, the magnetostructural coupling will be briefly discussed.

2.1.1 Structural and magnetic phases

There are three typical crystallographic structural phases for the $R_5(Si_{1-x}Ge_x)_4$ family: Orthorhombic I, or Sm_5Si_4 -like (Pnma space group); Monoclinic (P 1121/a space group); and Orthorhombic II or Sm_5Ge_4 -like (Pnma space group).

These structures can be seen as a successive stacking of slabs with nanometer height [3]. These slabs are composed by two alternate blocks of different polyhedral: a pseudo-cube with the rare earth atoms organized in a body centered cubic (BCC) structure and a pseudo-cube with the rare earth atoms disposed -also in a BCC type structure, with the exception of the center, where there is a pair of Si and Ge atoms. *Figure 1* shows such blocks. The majority of the compounds of the $R_5(Si_{1-x}Ge_x)_4$ family can assume all of these structures, at different temperatures and pressures.

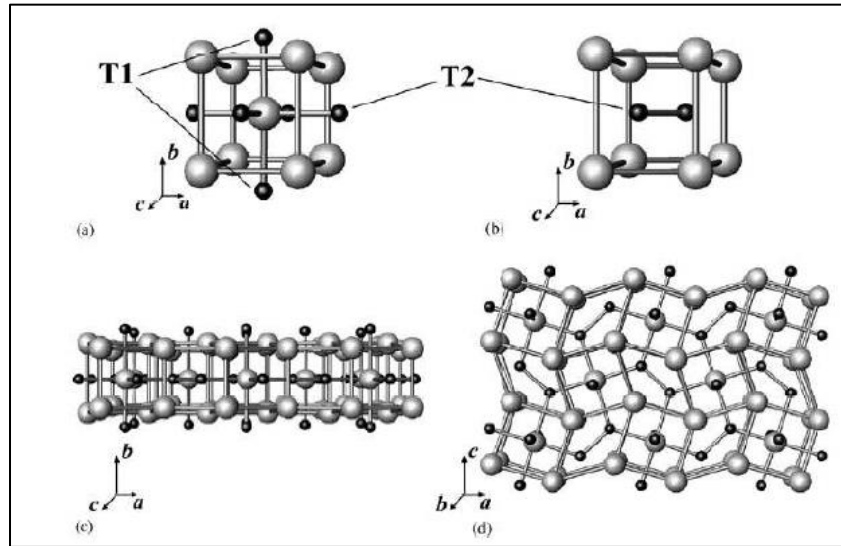


Figure 1 - (a) and (b) Illustration of the constituting blocks of the slabs of the $R_5(Si_{1-x}Ge_x)_4$ family. (c) is the perspective from the a-b plane, which represents a slab. (d) is the perspective of the a-c plane, showing the connection of adjacent slabs in the b direction [4].

The so-called T2-T2 connection is responsible for intraslab connections, and is occupied by Si/Ge atoms, creating a slab of infinite length and width in the a-c plane. The T1 sites are responsible for the interslab connections and for their stacking along the b direction. The three structural phases referred previously correspond to the number of T1 covalent bonds that are present in the crystal. So, the Orthorhombic II, or O(II) structure has no T1-T1 bonds between slabs, the Monoclinic (M) has half of the bonds and the Orthorhombic O(I) has all of the covalent bonds between slabs. *Figure 2* shows a scheme of the three phases and respective interatomic bonds, as well as a structural and magnetic phase-diagram of $Gd_5(Si_xGe_{1-x})_4$, depending on the temperature and Si concentration.

It can be seen that the ferromagnetic state/phase (FM) is only associated to the O(I) crystallographic structure, the paramagnetic (PM) phase associated to the (M) and O(II) structure and antiferromagnetic (AFM) phase is only associated to the O(II) structure. According to Choe and co-workers [4], [5], the effective exchange parameter, J_{eff} , is greater for shorter distances between atoms of Gd-Gd, which means that for the O(I) parameter, where all interslab bonds are present, the volume is smaller, so this parameter is larger (positive in this case), and so the magnetic coupling is higher, hence the ferromagnetic phase. On the other hand, the shorter (negative in this case) J_{eff} parameter is preferable for the (M) and O(II) structures.

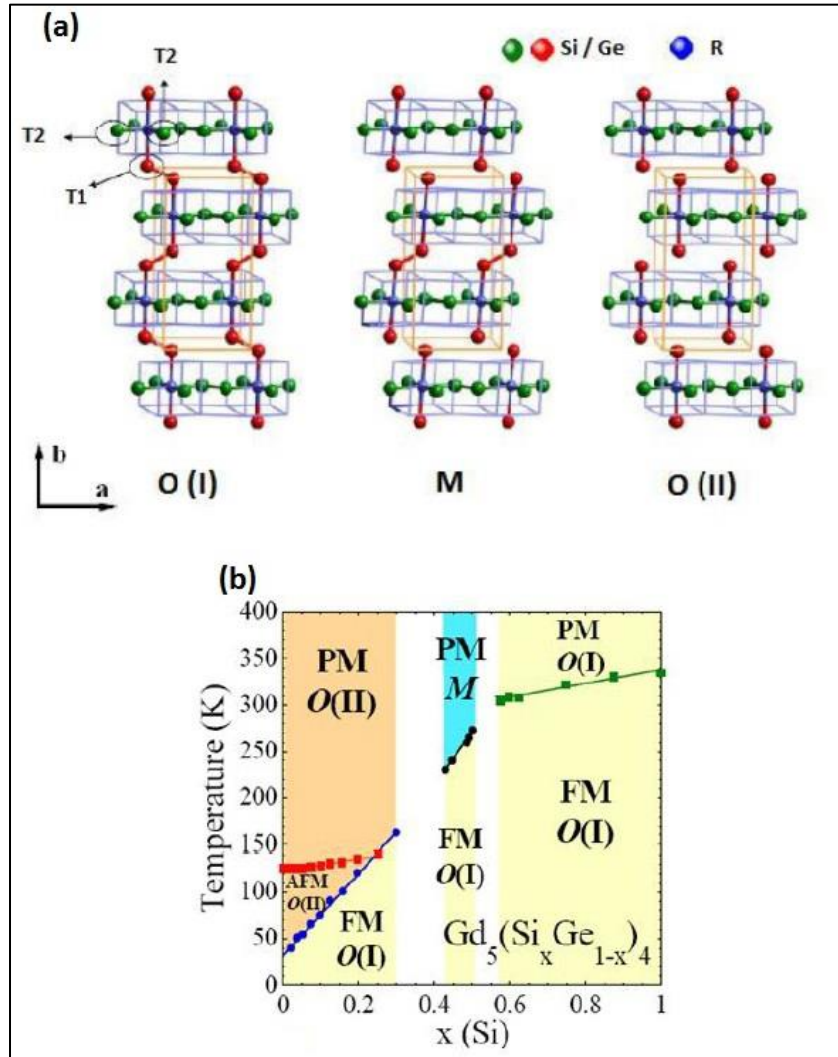


Figure 2 - (a) Possible structures of the $R_5(Si_{1-x}Ge_x)_4$, where the difference from each other is based on the number of T1-T1 interslab bonds existent. (b) a structural and magnetic phase-diagram of $Gd_5(Si_xGe_{1-x})_4$ for different temperatures and Si concentration is illustrated, delimiting the regions of different structural and magnetic phases [2], [4]

2.1.2 Phase transition and magneto structural coupling of $Gd_5(Si_xGe_{1-x})_4$

The magneto structural coupling is the simultaneous change of crystallographic and magnetic structures at a certain given temperature, T_s , favoring the structure with the lower free energy. T_s can be defined as the temperature above which one structure becomes more energetically favorable than other, this implies that at T_s $\Delta F_{min}[M] = \Delta F_{min}[O(I)]$. This change can also occur when a sufficiently high magnetic field is applied. The Giant Magnetocaloric Effect (GMCE) of $Gd_5(Si_xGe_{1-x})_4$ occurs,

precisely because the application of a high magnetic field, causes a transition from a [M, PM] state to a [O(I), FM] one [3]. The Magnetic field also promotes a more moderate $\Delta F(T)$ temperature dependence. It is possible, at room temperature, to promote the magneto structural transition by applying a sufficiently high magnetic field that allows the system to gain enough energy to overcome the free energy difference between the structures.

Figure 3 illustrates the free energy as a function of temperature, for both $Gd_5Si_2Ge_2$ and $Tb_5Si_2Ge_2$. In the case of $Gd_5Si_2Ge_2$, as A. L. Pires and co-workers reported [6], the magnetostructural transition from [O(I), FM] to [M, PM] occurs at 265 K. This simultaneous transition from both magnetic and crystalline structures occurs because the Curie Temperature for the M phase is around 209K (below T_S) and the Curie temperature for the O(I) phase is around 301 K (above T_S). That means that when the structural transition occurs from O(I) to the M phase, the respective magnetic phase transition also occurs to the magnetic phase of the Monoclinic structure, hence the simultaneous occurrence of the [M, PM] phase. The same cannot be said about $Tb_5Si_2Ge_2$.

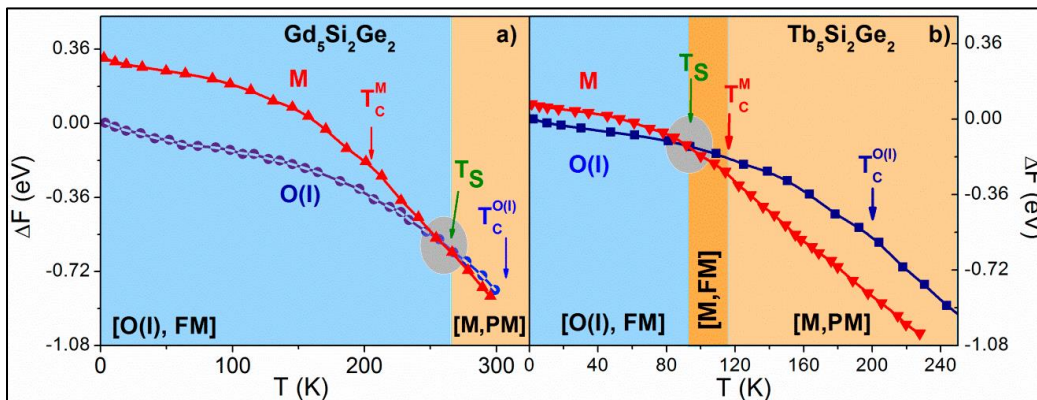


Figure 3 - Free energy as a function of temperature for both the (M) and O(I) structures, for the case of (a) $Gd_5Si_2Ge_2$ and (b) $Tb_5Si_2Ge_2$ [6].

As can be seen in figure 3, the structural critical temperature (T_S) is below both Curie temperatures. Therefore, when the structural phase change occurs, neither of the phases has changed magnetic ordering, and so the magnetostructural transition does not happen.

These structural transitions occur due to the sliding of adjacent slabs in the a direction (Figure 1) in opposite directions, generating lattice displacements. The interatomic distances in the a direction, the so called T1-T1 interslab connection distances, also change. The interslab distance increases with temperature, and when it is above the T_S , some of the connections are broken, originating the structure of the Monoclinic phase from the previous O(I) phase.

2.2 Laser matter interaction

Laser ablation of solid targets in liquids has gained substantial interest by the scientific community in the last decades due to its potential for practical and technological applications [7], as well for understanding the nature of the interaction between laser light and matter. Among the applications, it is possible to mention biomedical [8], chemical synthesis of new compounds [9], including nanocrystals, surface patterning and surface coating [10], etc.

Laser ablation was first reported in the 1960s, when ruby lasers were developed by Theodore H. Maiman and became more widely available. Since then, Pulsed Laser Ablation (PLA) has appeared as a new method of processing materials. In particular, Pulsed Laser Deposition (PLD) is one of many deposition techniques, and is based on PLA, where a laser beam interacts with a bulk material to form thin solid films, superfine powders, nanoparticles, etc. PLD is usually operated in vacuum or diluted gas ambient. When the medium surrounding the sample is a liquid, PLA gains the name of Pulsed Laser Ablation in Liquids (PLAL).

The pioneering work on PLAL was performed by Patil et al, where a bulk iron target was ablated underwater [11]. Kabashin et al [12] reported the synthesis of gold nanoparticles by laser ablation in water. Ogale and co-workers [13] managed to observe the metastable diamond phase from ablation of a graphite target immersed in liquid benzene, using a pulsed ruby laser.

Laser-matter interaction, ablation mechanisms and other general processes of light interacting with matter will be summarized in this section. Also, a comparison between femtosecond and nanosecond pulsed laser ablation will be made, comparing processes associated to each type of ablation, advantages/disadvantages, among others.

2.2.1 Ablation mechanisms

According to *Tan et al.* [14] there are five main ablation processes to consider: spallation, phase explosion, spinodal decomposition, Coulomb explosion, fragmentation and vaporization. These processes have a large dependence on the incident fluence of the laser beam. *Figure 4* shows the typical values of laser fluence for each process, as well as a diagram of temperature as a function of density and the typical Femtosecond Laser Ablation in Solution (FLAS) paths. Each of these processes will be approached superficially, only to allow a basic understanding of the mechanisms responsible for the ablation process.

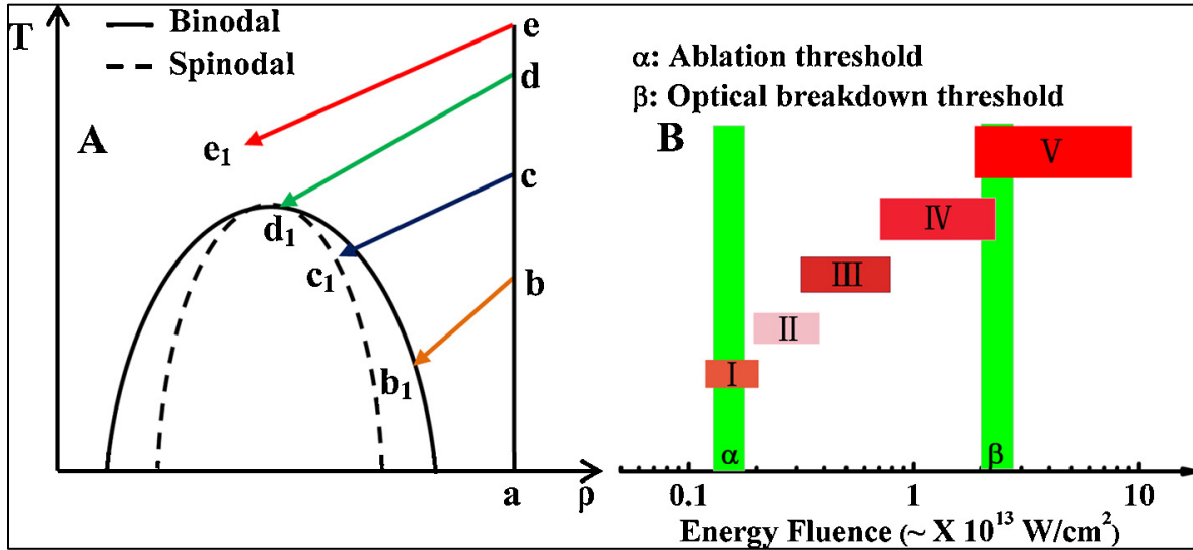


Figure 4 - (A) Schematic temperature (T)-density (ρ) phase diagram and typical FLAS paths ($b \rightarrow b_1$, $c \rightarrow c_1$, $d \rightarrow d_1$ and $e \rightarrow e_1$). (B) Possible mechanisms as a function of fluence. I: Spallative ablation; II: Phase explosion ablation, III: Spinodal decomposition, IV: fragmentation and vaporization, V: Plasma ablation and Coulomb explosion. α : ablation threshold. β : optical breakdown threshold (plasma formation threshold) (after [14])

Spallation: this process results from internal failure caused by the generation of defects, which are caused by tensile stresses [14], [15]. It is basically the fracture of a solid when the tensile strength is exceeded. After isochoric heating of the target via ultra-fast multiphoton absorption, two compressive waves are created and propagate through the liquid and the solid target, in order to relax the thermoelastic energy accumulated (path b to b_1 in *Figure 4 A*). These waves induce fractures parallel to the target surface. The interaction between the compressive waves and the solid-liquid interface creates tensile stresses, pushing the ablated materials away from the bulk target. During this process, voids are created near the surface, and in time they grow, nucleate and coalesce. Thus, an entire layer can be ejected from the surface of the material, and eventually it breaks up as the distance to the bulk increases. It is by this fragmentation of expanding layers that nanoparticles can be created. This mechanism usually occurs in a narrow range of incident laser fluence around the ablation threshold. When the fluence increases, the amplitude of the tensile waves decreases, and other mechanisms take a more important role. *Figure 5* illustrates the process of spallation.

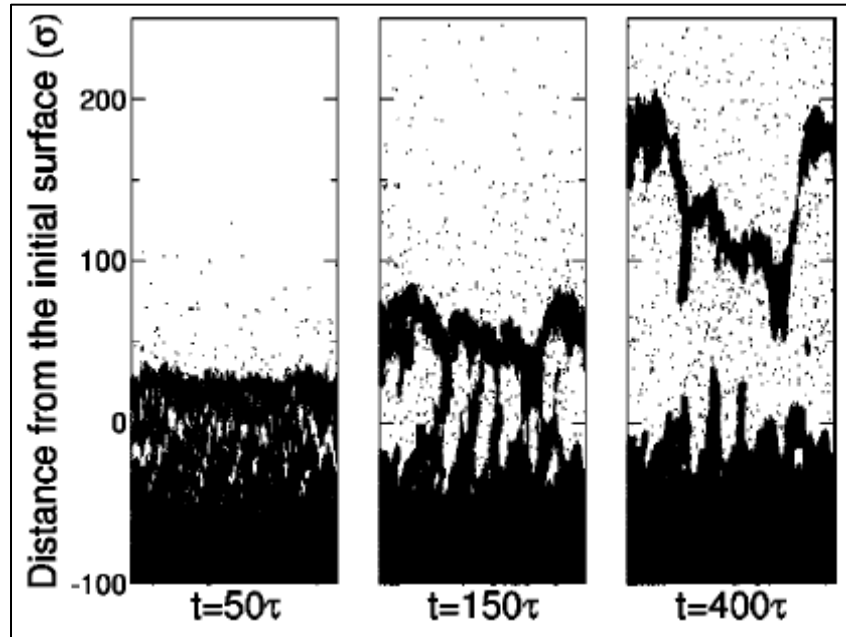


Figure 5 - Spallation process [15]. The times in the image are characteristic times, used in the model of the author (D. Perez). Note: this image is used only for descriptive purposes. After characteristic times defined by the author, it can be seen the complete removal of a layer of material from the target surface. From the image on the left it is possible to see the voids created, and as time progresses, these voids will increase until the ejection of the layer.

Phase explosion: this process (also called explosive boiling) occurs when the incident fluence is well above the ablation threshold (*Figure 4 B*). This mechanism is characterized by a homogeneous bubble nucleation near the so-called spinodal temperature (which depends on the material), slightly below the critical temperature (path c to c1 in *Figure 4 A*), where the liquid near the target surface makes a rapid transition from superheated liquid to a mixture of vapor and liquid droplets [16]. In this case, superheating means that the liquid temperature rises so fast that it passes beyond the normal boiling temperature (T_b), therefore being metastable. The spinodal temperature is the temperature limit at which the metastable liquid can be heated, without evaporating [16]. Basically, what happens is that the material ablation is induced by the rapid disintegration of the superheated liquid, and nanoparticles are formed from the subcritical material. *Figure 6* illustrates time-resolved reflectivity images of silicon and germanium targets during phase explosion, with different delay times. It can be seen that as time progresses after the incidence of the laser, the explosion front expands away from the central spot of incidence. The delay time observed indicates that this process is of thermal nature, as the expansion front is registered in the ns time regime.

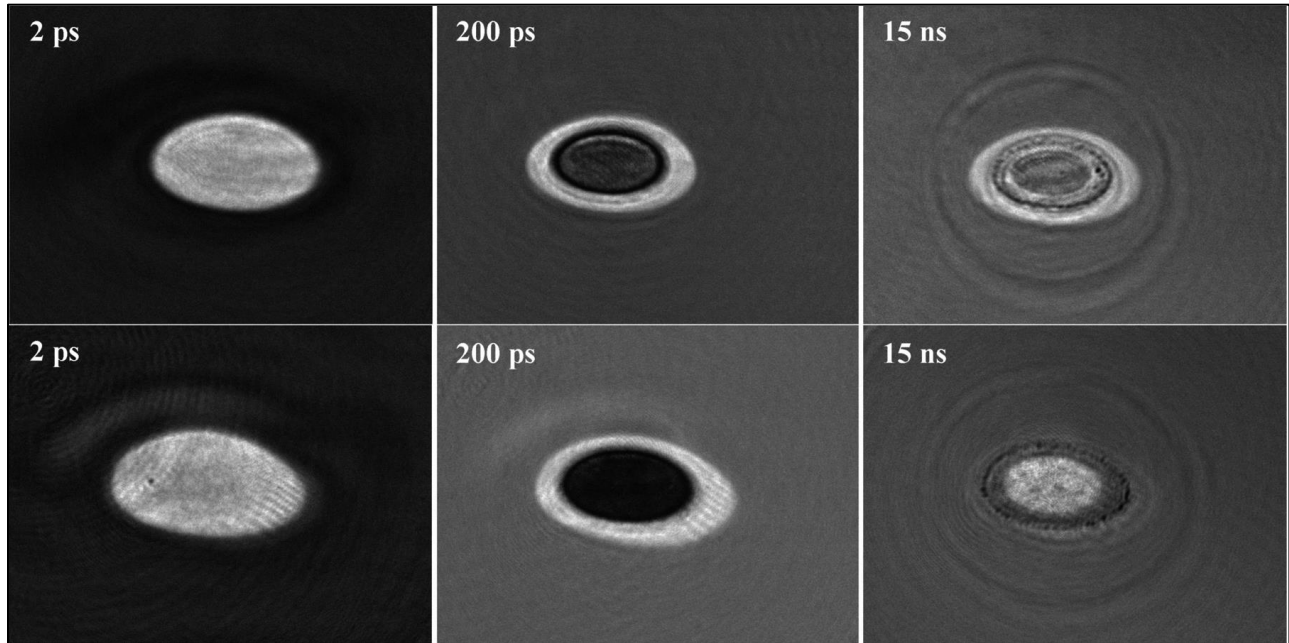


Figure 6 - Time-resolved reflectivity images of silicon (upper row) and germanium (lower row) at different delay times. The laser parameters are $\lambda_{\text{pump}} = 400 \text{ nm}$, 120 fs pulse, $1.4 \text{ J}\cdot\text{cm}^{-2}$. Frame size is $126 \times 95 \mu\text{m}^2$ (after [17])

Spinodal Decomposition: For higher laser fluences (*Figure 4 B*), spinodal decomposition is another mechanism for laser ablation, by which an alloy or mixture decomposes into equilibrium phases. It occurs when there is no thermodynamic barrier to the decomposition, and thus operates solely by diffusion [18]. With laser fluence injected in the material, heating directly above the critical temperature, the subsequent expansion creates a thermodynamically unstable region, causing material decomposition [14] (path d to d₁ in *Figure 4 A*). Changrui Cheng and Xianfan Xu [19] performed simulations based on a two-temperature molecular dynamics model, whose results are illustrated in *Figure 7*.

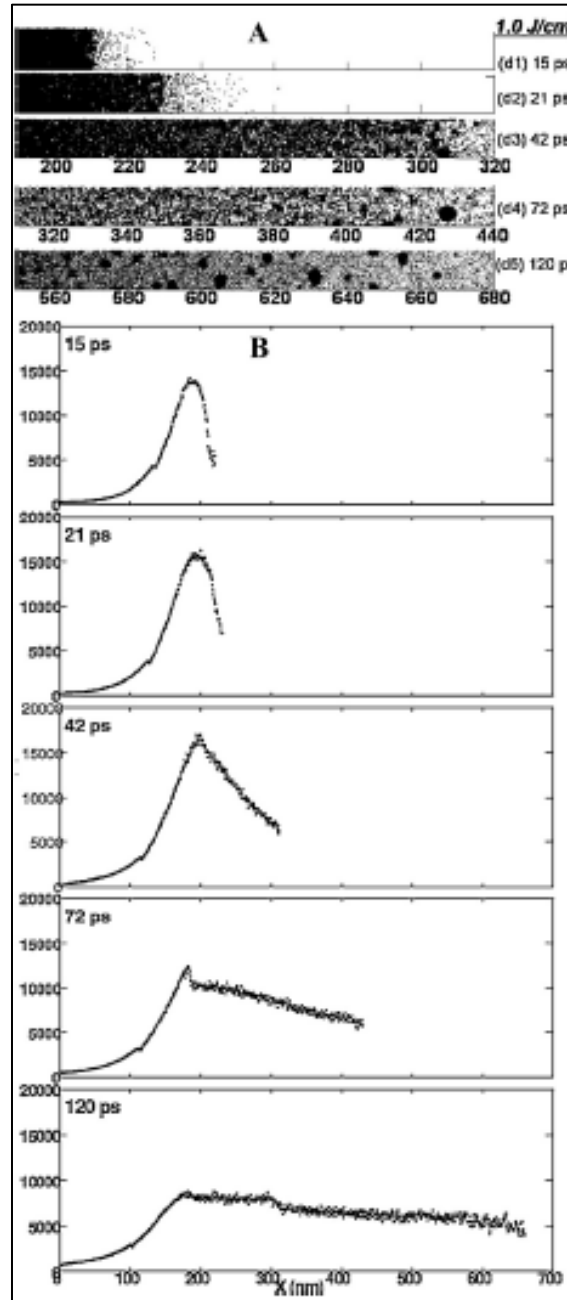


Figure 7 - (A) Snapshots of the ablated area, and (B) Temperature spatial distribution for different time steps (image presented in [14], which was in turn adapted and with permission from [19])

Figure 7 A shows that from the initial homogeneous phase, appears a mixture of liquid droplets and gas atoms. As time moves forward, the liquid droplets coalesce in bigger clusters, while some atoms still remain in the gas phase. Figure 7 B represents the simulation of temperature distributions throughout layer thickness for different time steps. It shows that the peak surface temperature exceeds the critical temperature, and that the surface temperature is also lower than the interior one

[14]. All these results in phase spatial separation are due to overall temperature, pressure and density gradients. The resulting particles are cooled very fast and adiabatically, forming bubbles and droplets transition layers [14], [19], [20].

Fragmentation and vaporization: fragmentation and vaporization can be distinguished in 2 ways: the so-called “trivial” and “nontrivial” one [14], [15], [21], [22]. “Trivial” fragmentation occurs when the expansion of the superheated volume can produce enough energy in the supercritical fluid, leading to decomposition as a result of impact or expansion (path e to e1 in *Figure 4 B*), and fragments are formed. Nanoparticles can be formed from these fragments by subsequent collision and aggregation. On the other hand, “Nontrivial” fragmentation occurs when the expansion is so fast that the superheated material brakes the equilibrium structure by atomic diffusion, and a nonequilibrium structure appears from the transition of a homogeneous to a heterogeneous fluid in the expanding matter region, resulting in the formation of a clustered phase [14], [22]. Finally, vaporization occurs when, under higher incident fluence, the surface layer of the target is atomized and expands at very high speed [14], [15], [21]. *Figure 8* illustrates a scheme of the ablation process, and a scanning electron microscopy (SEM) image of an ablated area [23]. As it can be seen, there is no evidence of molten material, and only dust exists around the hole. This means that thermal processes are not occurring in a relevant way, and only ablation from vaporization and non-thermal processes is present [14], [23].

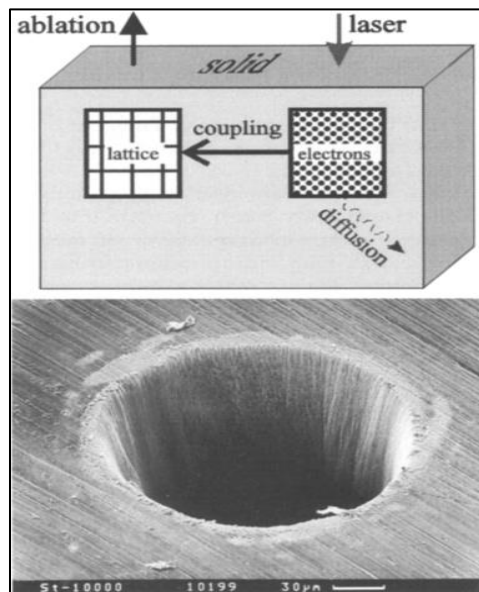


Figure 8 - A scheme of FLA and a SEM image of an ablated area. From the image, one can see that non-thermal processes are present due to the lack of molten material [23]. Laser parameters are 200 fs, 120 μJ , $F = 0.5 \text{ J}\cdot\text{cm}^{-2}$ with wavelength of 780 nm. Hole thickness is 100 μm

Coulomb explosion: finally, the Coulomb explosion occurs for laser fluences above the plasma formation threshold (*Figure 4 B*), where a transition from the solid state to plasma is achieved [7], [12], [14]. Coulomb explosion occurs when excited electrons are ejected from the target surface, either by photoelectric or thermionic emission, creating a strong electric field between the excited electrons themselves and the highly ionized ions of the target material, being known as the space charge effect [24]. Of course, this charge separation only occurs when the received energy from laser photons exceeds the Fermi energy. If the electron energy is greater than the ion binding energy to the lattice, then layers of material will start to be removed from the bulk, due to the strong electric field created by the charge separation. After tens of picoseconds, a plasma plume appears, consisting of electrons, atomic and ionic species from the target and liquid, and is created by direct ionization, sublimation and electron emission [24]. When the plasma plume expands, it creates a laser-induced shock wave, as illustrated in *Figure 9*. The red dotted line depicts the shock wave front.

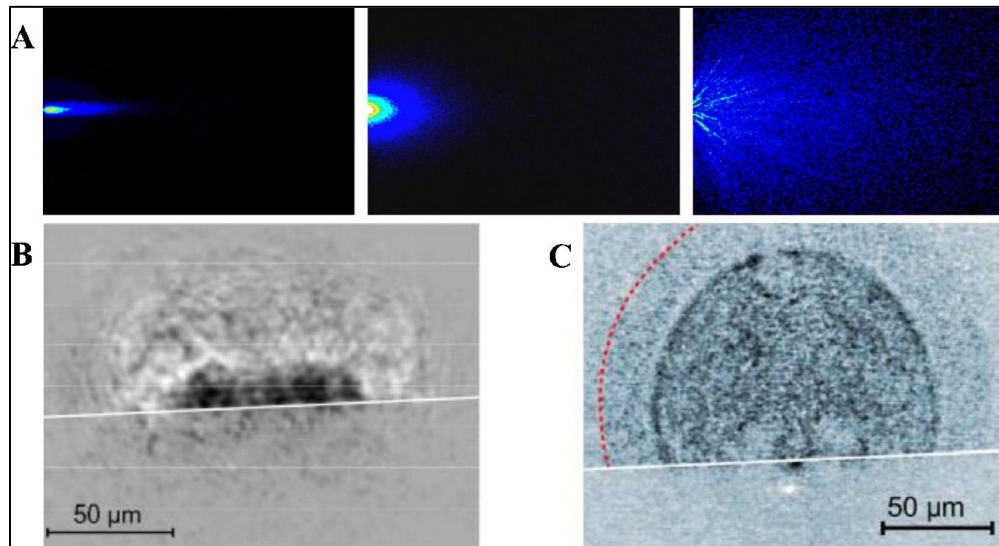


Figure 9 - (A) Images taken from a CCD camera of the plasma plume induced by femtosecond laser irradiation of a Titanium target. The images are recorded at various delay time after the femtosecond laser pulse for different camera gates depending on the intensity of the signal. (B) Shock wave propagation 4 ns after the ablation pulse with a probe wavelength of 400 nm and (C) 90 ns after the ablation pulse with a probe wavelength of 525 nm (image included in [14], which in turn was adapted with permission from [25], [26])

For even higher fluences, well above the plasma formation threshold ($>10 \cdot 10^{13} \text{ W} \cdot \text{cm}^{-2}$ in *Figure 4 B*), melting occurs, and it creates a zone with broad and irregular profile [14], [27]. *Figure 10* shows such melting zone.

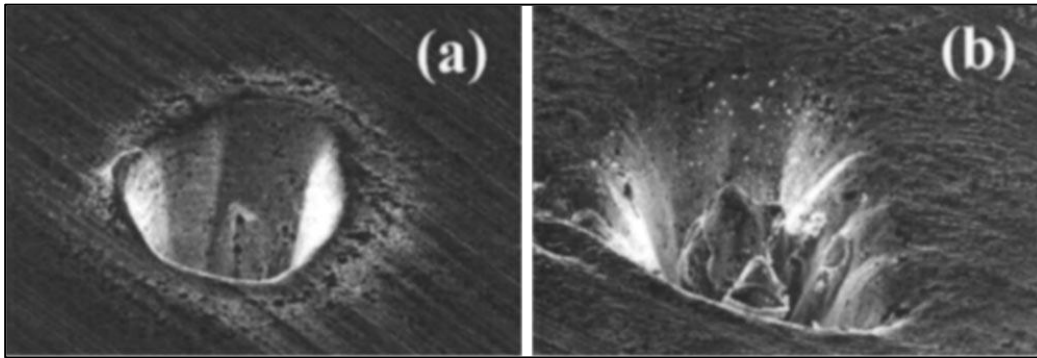


Figure 10 - Craters in the surface of a gold target after 5000 pulses at (a) $F = 60 \text{ J}\cdot\text{cm}^{-2}$ and (b) $F = 1000 \text{ J}\cdot\text{cm}^{-2}$ [27]

2.2.2 Femtosecond laser ablation of dispersed powders in solution (FLAS)

Besides laser interaction with the target itself, we can also consider the case where the laser beam interacts with the ejected material. This is called FLA of dispersed powders in solution. There are mainly three mechanisms that can cause the generation of nanoparticles: photothermal ablation, the already mentioned Coulomb explosion and near-field enhancement [14], [28], [29].

1 – **Photothermal ablation:** for low fluence and high laser repetition rate, photothermal ablation may occur. Due to nonlinear absorption, originated from the high repetition rate, multiphoton absorption occurs. The resulting charge repulsion could result in melting, and nanoparticles can be created through surface evaporation [14], [29].

2 – **Coulomb explosion:** increasing fluence, Coulomb explosion takes place [14], [28], [29]. Werner et al., for example, stated that nanoparticles of gold with 60 nm size melt totally, due to high thermionic electron emission. This thermionic emission is responsible for the fragmentation of nanoparticles in smaller ones, because of the repulsion of the positive e^+ charged ions caused by the Coulomb explosion. Werner states that is more likely to occur Coulomb explosion in the liquid nanoparticles, rather than the solid ones.

3 - **Near-field enhancement:** near-field enhancement mechanism has been proposed by Anton Plech and co-workers for ablation [30]. This mechanism works in the proximity of small metallic nanoparticles on a surface, due to optical near-field effect. At edges with high curvature, the evanescent field can be enhanced by several orders of magnitude in comparison with the incident field.

Figure 11 depicts the 3 processes described above.

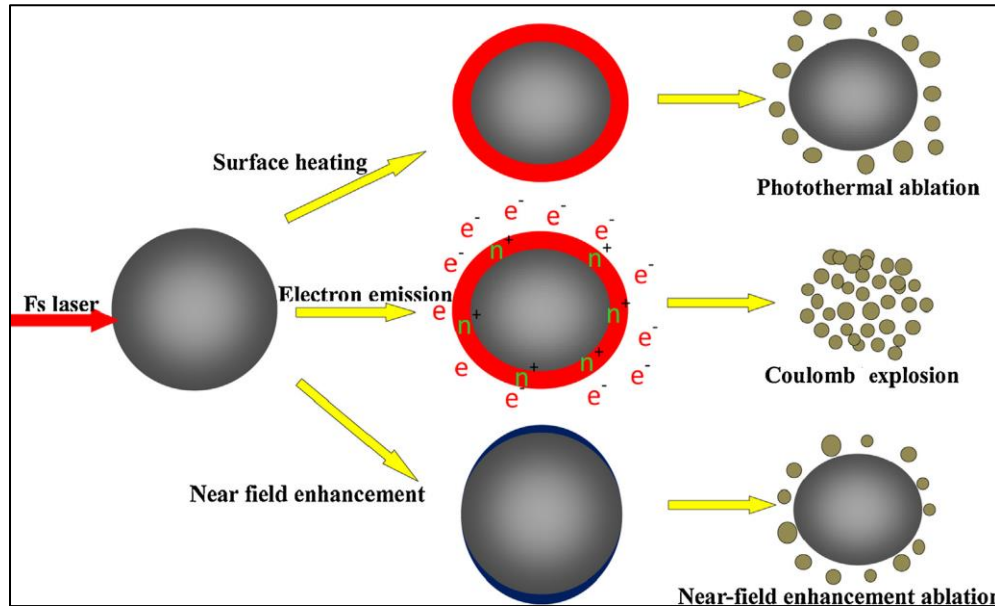


Figure 11 – Mechanisms of FLAS of dispersed powders in solution. In sequence, from top to bottom: photothermal ablation by multiphoton absorption and consequent heating, resulting in melting; Electronic emission, creating the charge repulsion that originates Coulomb explosion; Near field enhancement (after [14])

2.2.3 Experimental parameters

Besides general interactions between laser radiation and matter, other parameters are important for the production of nanoparticles, such as the characteristics of the used laser, target material, and solution parameters. The final average size, size distribution, crystallographic and magnetic structure of the fabricated nanoparticles depend strongly on these parameters. This section refers some examples of the influence of these parameters on the final results.

Laser parameters: Laser parameters have a very important role in NPs fabrication. In particular, the repetition rate. Barcikowski and coworkers [31] reported a linear increase in the amount of nanoparticles produced with the increase of the repetition rate from 100 to 2500 Hz. In addition, with increasing repetition rate, the resultant nanoparticles are smaller, and have a narrower size distribution, as well as fewer agglomerates produced. Moreover, the laser irradiation after ablation induces fragmentation by the above discussed mechanisms, which reduces the size of the already ablated material. Moreover, the repetition rate not only influences size, but also the structure of the resultant NPs. A. Santagata and co-workers reported the production of diamond-like carbon (DLC) and nanodiamond structures, with repetition rates ranging from 10 to 100 Hz for DLC and 1kHz for

nanodiamond [32], with a 100fs laser pulse in water environment. They state that for 1kHz laser repetition rate, the water cavitation bubbles expansion could lead to adequate conditions of physical-chemical nature and are responsible for the nanodiamond particles growth. On the other hand, for repetition rate of 10-100 Hz, these properties cannot be achieved, and the metastable diamond-like phase is obtained instead. Pulse duration is another important parameter, according to Riabinina et. al. [33], whose work consisted on the ablation of a gold target in liquid media, where increasing the pulse duration from 40fs to 150fs does not change the productivity of the ablation, translated as the amount of material ablated. For pulses longer than 150fs, the productivity increases, to reach a maximum at 2ps, where it is 100 times higher than the 40-150 fs regime, and from this maximum it starts to decrease significantly. For pulses longer than 2ps, the heat conduction starts to take place and a large fraction of the incoming laser energy is absorbed by the expanding plume. At this point, the energy only assists ablation at late times, decreasing the ablated volume of material. Furthermore, laser wavelength is also important, because the absorption coefficient of materials is strongly dependent on it [14]. Absorption coefficient is higher for shorter wavelengths in most of the cases, so smaller nanoparticles should be produced in this case. Akman and co-workers [34] studied the effect of different wavelengths on Ag nanoparticles produced in liquid media. Initially the Ag target immersed in sodium dodecyl sulfate (SDS) was irradiated with 800nm irradiation at 1 kHz repetition rate, with a post treatment that consisted of irradiating the resulting solution separately with 800nm and with the harmonic of 400nm, 48 hours after the initial ablation. From the initial solution the average nanoparticle size was 142nm. After the post treatment, the average sizes measured were 11 nm and 22 nm, for the 400 nm and 800 nm irradiation, respectively.

Material properties: concerning the material properties, different parameters like density, absorption spectrum, melting and boiling temperature, atomic species, phase diagram, etc., mixed with the above laser parameters, lead to different types of nanoparticles. Nanoparticles can have the same composition and phase as their bulk counterpart. This is usually observed in noble metals, due to the high cooling rate of the plasma plume and low reactivity. It can also happen that the new nanoparticles can have different composition and/or phase than the target. As already mentioned above, there is the case of diamond-like carbon, a metastable phase of diamond, and nanodiamond [32].

Solution parameters: regarding solution parameters, they are essentially induced by cavitation. Its PLA properties like volume, lifetime, and expansion affect nucleation and growth processes of the produced nanoparticles, and also can determine the final structure [14], [35]. When the ejected material reaches the liquid, the target particles get trapped in the induced cavitation

bubbles. These bubbles differ in size, depending on the compressibility of the solution. Slow compressible solutions mean higher collision probability, therefore aggregation of bigger nanoparticles, and vice versa. As previously mentioned, among the materials parameters, the reaction between the ablation target and the involving liquid might create different materials, with different compositions, structures, properties, etc, from the initial ablated target [14]. By changing the solution, we can also change the resulting structures and properties of the new fabricated nanomaterials.

2.2.4 Liquid confinement, thermodynamic and kinetic properties

According to G. W. Yang [7], there are three fundamental aspects to consider when talking of pulsed laser ablation in liquids: liquid confinement, thermodynamic and kinetic aspects. In this section, they will be approached.

Liquid confinement: liquid confinement is an important aspect of laser ablation in general. After the laser incidence and posterior ejection of material, the laser-induced plasma expands adiabatically at a very high speed. This supersonic ejection of material will create a shockwave due to the liquid confinement and continuous expansion of the ejected species, as well as the interaction between both the laser beam with the target material and the later part of the beam with the already ejected particles [7]. This shockwave will be responsible for an increase in pressure in the plasma. Due to liquid confinement, this extra pressure will lead to an increase in temperature, and a thermodynamic state of high temperature and pressure, as well as high species density. This state is favorable for the formation of metastable phases present in the thermodynamic equilibrium phase diagram, at the extremum regions of temperature and pressure. Since ablation occurs in a liquid environment, chemical reactions occur between the plasma plume and the surrounding liquid. There are basically four types of chemical reactions that can occur during the ablation and plume expansion. The first is inside the plume itself, where the high temperature (T) and pressure (P) are favorable for the formation of new phases, which result from the species and the target material. The second type of reaction occurs inside the plume, but this time with the species created at the liquid plasma, resulting from the high temperature and pressure states of the plasma plume from the target, which evaporates the liquid molecules that are near the frontier between target plasma and liquid. This liquid plasma is called plasma-induced plasma (PIP) [7], since it is the laser induced plasma (LIP) and not the laser beam itself that directly originates it. The third kind of process occurs at the interface between the LIP and the liquid. The main difference from the second type is the state or phase of the liquid species involved in the reaction, which in this case have not been evaporated. The fourth

reaction takes place inside the liquid itself. Due to high pressure in the plasma front, the material ejected species are pushed from the plasma-liquid interface directly to the liquid, where such reactions occur. Because of these different possible reactions, nanomaterials engineering and fabrication are possible, and several combinations of different materials and properties can be explored in the high Temperature and Pressure regimes [7], [36], [37]. The last stage of the plume is its condensation after cooling down. Basically, there are two ways of condensation: the particles that were not pushed into the liquid in the fourth type chemical reaction, or the ones that are large enough, are condensed and deposited on the target surface. This process can be used as a way of coating the target surface with a metastable phase of the material itself, or as a way of film deposition in the bottom surface of the liquid container [7], [38]-[40]. It is worth to point out that the smaller particles condensate and float on the top surface of the liquid, due to the large surface tension [7].

Figure 12 illustrates the process of the plasma plume phases, involving the creation, expansion, reactions, condensation, etc.

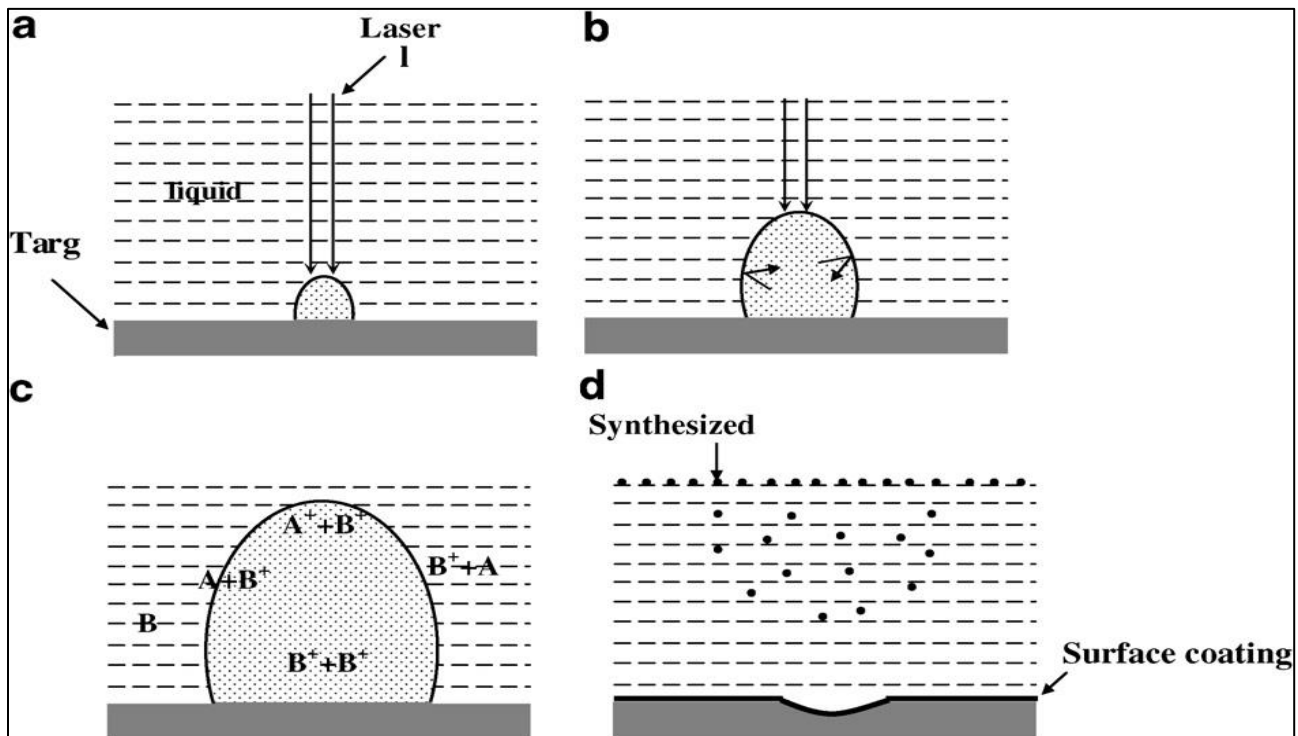


Figure 12 – 4 steps of plasma plume evolution in PLAL: (a) creation of the plume due to the incidence of the laser energy; (b) expansion of the plume ; (c) chemical reactions between target material and surrounding liquid, during the plume expansion; and (d) plasma plume condensation, either floating to surface (smaller nanoparticles) or condensation in the bottom of the liquid (larger nanoparticles) (after [7])

Thermodynamic aspects: The thermodynamic aspects of PLAL can be studied with respect to three distinct parameters, stated previously, namely: temperature (T), pressure (P) and density of species (ρ). The density of species in the laser-induced plasma plume can be estimated by measuring the volume of the hole created at the target surface, and also measuring the volume of the plume, more specifically the volume of the light emitting region. From the images of the light emitting region, like the one in *Figure 13* (for an ablation of a graphite target in water), one can assume a plume to have the shape of a semi hemisphere, with diameter equal to the Full Width Half Maximum intensity (FWHM). Then, the next step is to estimate the volume of material ablated from the target surface, and from these two values the density of species present in the plume is estimated.

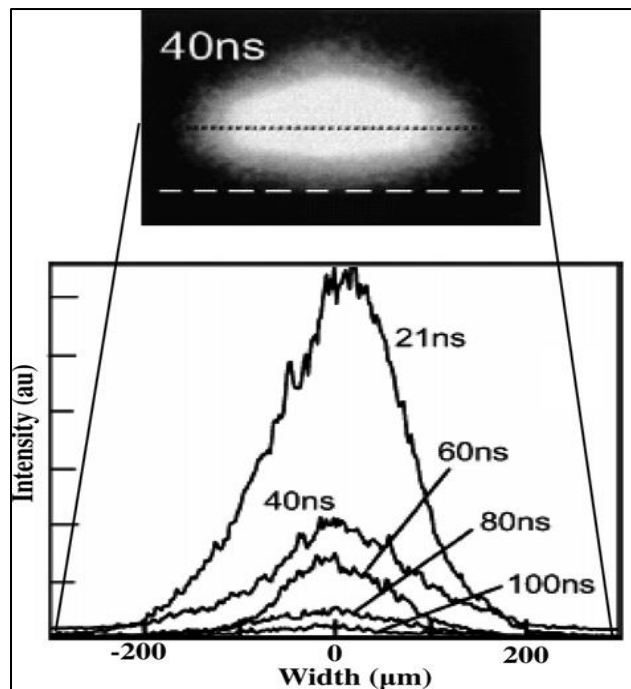


Figure 13 - Image of plasma plume light emitting region and respective intensity distribution from the ablation of a graphite target in water, using a Nd:YAG laser with wavelength of 1064 nm, a pulse duration of 20 ns, and fluence of $10 \text{ J}\cdot\text{cm}^{-2}$ (as exposed in [7] and its references)

An effective method for monitoring the temperature of the plasma plume is through the optical emission spectra [7]. Sakka and co-workers have obtained a 5000 K temperature for the laser-induced plume by optical emission spectra of C2 molecules, by ablating a graphite target in water with a Nd:YAG laser with 1064 nm wavelength, 20 ns pulse width, and 30 mJ pulse energy (fluence of $10 \text{ J}\cdot\text{cm}^{-2}$) [7], [41]. Close values of temperature were obtained for Ag immersed in water [42]. Laser induced plasma at high pressure can usually be attributed to two contributions: from the adiabatic

expansion of the plume after laser incidence and the extra pressure from the posterior shockwave. Pressures as high as 5.5 GPa have been measured by Berthe and co-workers [43], with a wave pulse duration of 50 ns, when a pulsed laser with 1064 nm wavelength, 20 ns pulse length and $10 \text{ GW}\cdot\text{cm}^{-2}$ power density irradiates an aluminum plate in water. Fabbro and co-workers (referred in [7]) even developed experimental techniques to measure the pressure by characterization of the shock waves generated by the ablation, as is illustrated in *Figure 14*.

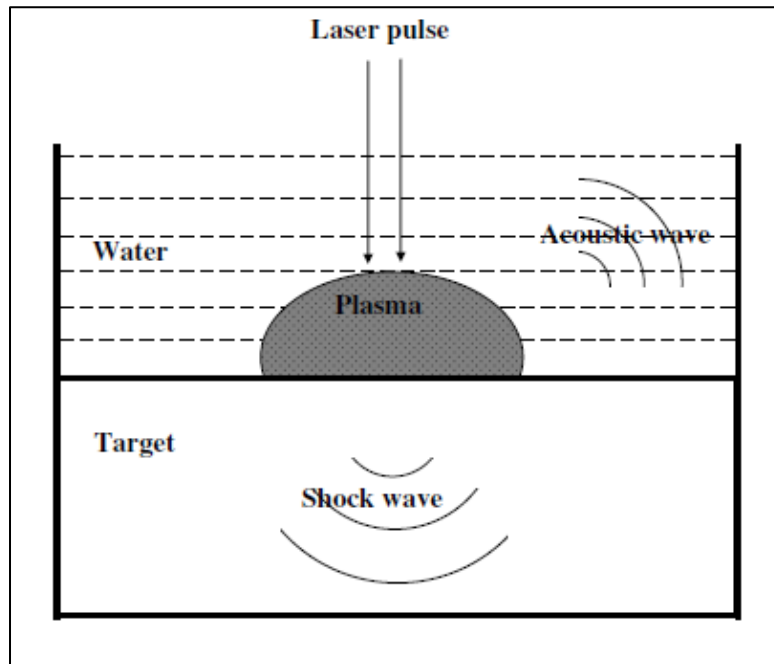


Figure 14 - Illustration of the recording of an acoustic wave generated in water and the shock wave in the target, to measure the pressure generated at the plume (after [7])

Kinetic aspects: main kinetic aspects include ablation rate and quenching. With the high temperature, high pressure and high-density plasma, additional continuous etching of the solid target is possible, increasing the ablation rate. Besides, ablation rate changes with the liquid thickness, as Zhu and co-workers have reported by ablating a Si target using a KrF excimer laser, with a pulse duration of 23 ns [44], [45]. With these parameters, the ablation rate was highest for a water layer thickness of 1.1 mm [44], as shown in *Figure 15*. As can be noted, there is an optimal water layer thickness with a maximum of ablation rate. There are two phenomena that are usually considered responsible for this maximum ablation rate, namely: 1) the shock wave generated by the plasma plume and emitted into the water and 2) the plasma inducing an explosion in water. After being emitted to the air layer, the shock wave decays in acoustic waves by air friction [7], [44]. This is called

the “ablative piston” effect, and it can greatly enhance the ablation process resulting from the high pressure and high temperature etching. This process is favorable for water layer thicknesses below the maximum point. For bigger layers of water, the laser energy is absorbed through the optical path inside the fluid, reducing the beam fluence that reaches the target. Therefore, a balance between these two phenomena are required for optimization of PLAL ablation rate process. Also, in the same work, *Zhu et al.* tested the amplitude of recorded shock waves as a function of water layer thickness. *Figure 16* shows the obtained results. Both ablation rate and amplitude of recorded waves show the same behavior, which means that increasing water layer thickness reduces considerably the amount of energy that reaches the target.

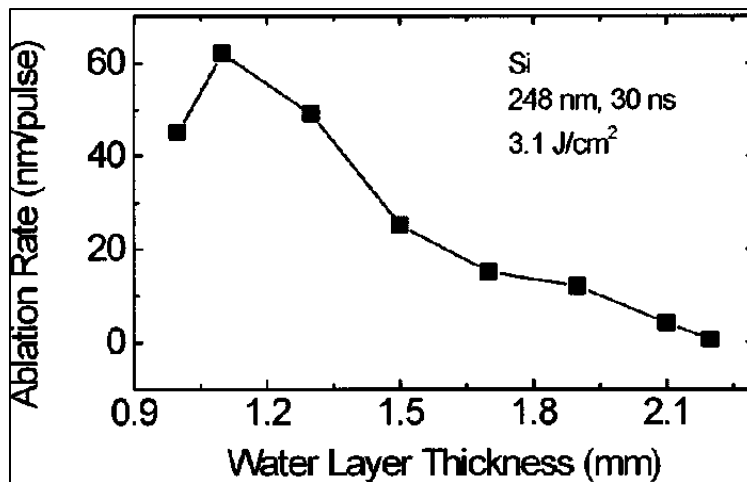


Figure 15 – Si laser ablation rate depending on water layer thickness, for a laser fluence of $3.1 \text{ J}\cdot\text{cm}^{-2}$ (after [44])

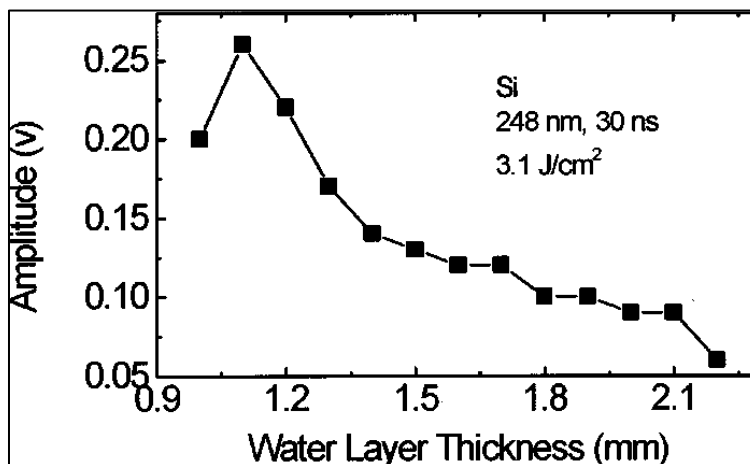


Figure 16 – First peak-to-peak amplitude of the recorded acoustic wave, depending on water layer thickness, for a fluence of $3.1 \text{ J}\cdot\text{cm}^{-2}$ (after [44])

Secondly, the short quenching time can limit the size of the nanoparticles produced, not giving time or energy to aggregate the species at the plume. According to *Yang et al.*, the size distribution of all small particles is at the nanometer scale when pulses with duration of less than 20 ns are used for PLAL [7]. The cooling effect adjacent to short quenching time can also take a role in the formation of metastable phases during plasma transformation. Basically, these phases can be frozen due to short quenching times. An interesting example is the formation of intermediate phase on the transformation of graphite to cubic diamond by ablating a graphite target in water [7], [46].

2.2.5 Nanocrystal formation

In this section the nanocrystal formation aspects will be discussed. Such aspects or processes include nucleation and kinetic growth. These processes will be discussed superficially, with some examples to illustrate them.

Nucleation: Nucleation from a parent phase to a stable one is a universal phenomenon in gas condensation, liquid evaporation, and crystal growth [7]. This process usually occurs during the transformation and condensation of the plasma plume. The theory supporting thermodynamic nucleation is based in two assumptions: 1) the nuclei of the particles formed are perfectly spherical and 2) that every nuclei does not interact with others. Also, the nucleation and phase transformation are described through the Gibbs free energy [7], [47]. Between competing phases, those that present lower or minimum Gibbs free energy are the stable phases, and those that require more energy are the metastable ones. For example, graphite and diamond phases can coexist at certain thermodynamic conditions, but the stable one is graphite [7]. Graphite phase transformation to diamond phase can be possible by giving enough energy to the system, in the form of pressure or/and temperature. As it can be seen in *Figure 17*, both critical radius and Gibbs energy increase with increasing pressure and reduces with increasing temperature. As an example, nanoparticles with particle size around 2-3 nm can be produced in the 4500K and 10 GPa region in the diamond phase. These values have been achieved by *Sakka et. al.* [42] and *Peyre et al.* (referred in [7]), thus enabling the production of one of the most precious and rare materials available today.

Kinetic growth: According to Yang, there are four main stages during kinetic crystal growth, including physical and chemical processes: 1) the ablation phase, where the plasma plume is created at the solid-liquid interface, with the pressure and temperature increasing to their respective highest value; 2) the condensation of the plasma plume, resulting in the formation of clusters by atomic diffusion and collision, until the clusters reach the size of critical nucleation, in the respective phase

transition; and 3) an approximate steady state growth of the nanocrystals by aggregation of smaller particles. This growth eventually decreases due to the pressure and temperature continuously dropping. C. X. Wang and co-workers obtained a relationship between temperature, pressure and nucleation time for graphite to change phase to diamond. The results are illustrated in *Figure 18* and as can be seen, the nucleation time increases with the temperature and decreases with pressure.

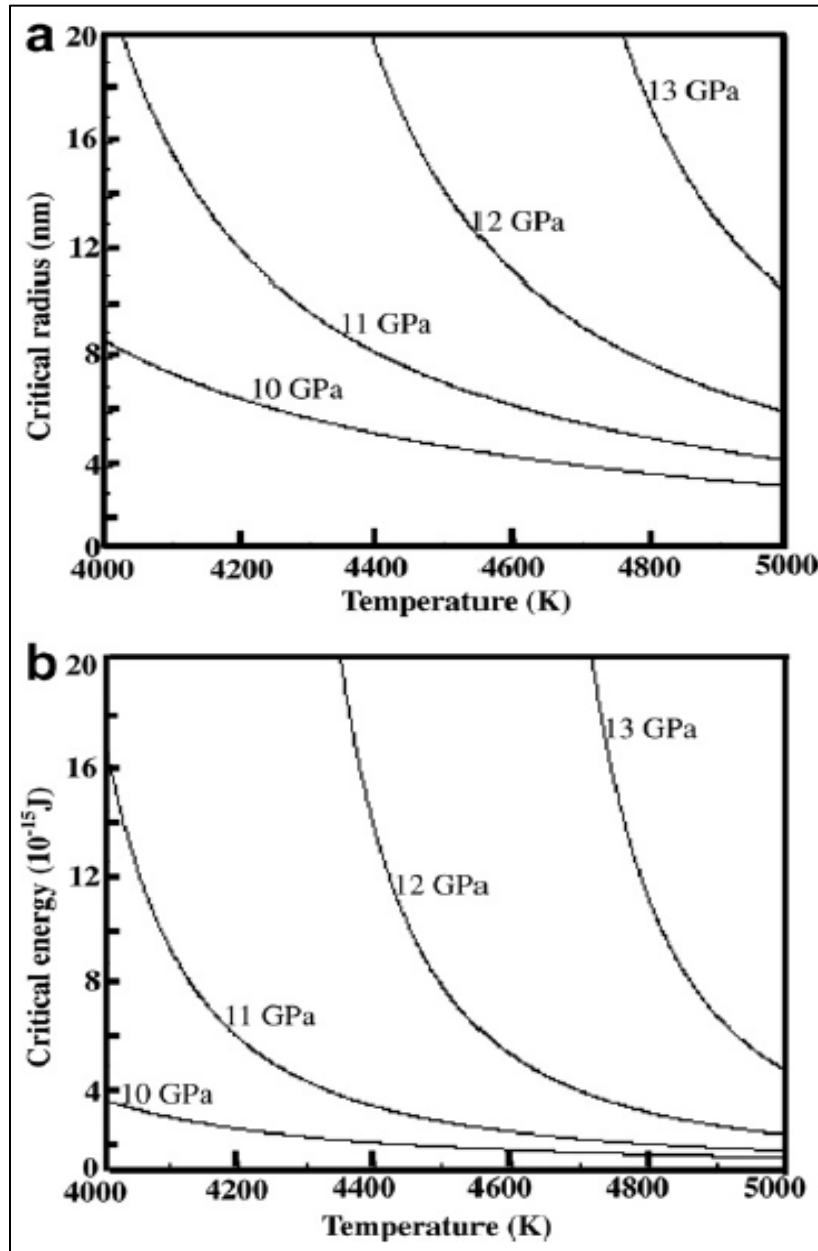


Figure 17 - (a) Critical radius r^* and (b) Gibbs free energy $\Delta G(r^*)$ of diamond critical nuclei dependence on the temperature for various values of pressure (as exposed in [7])

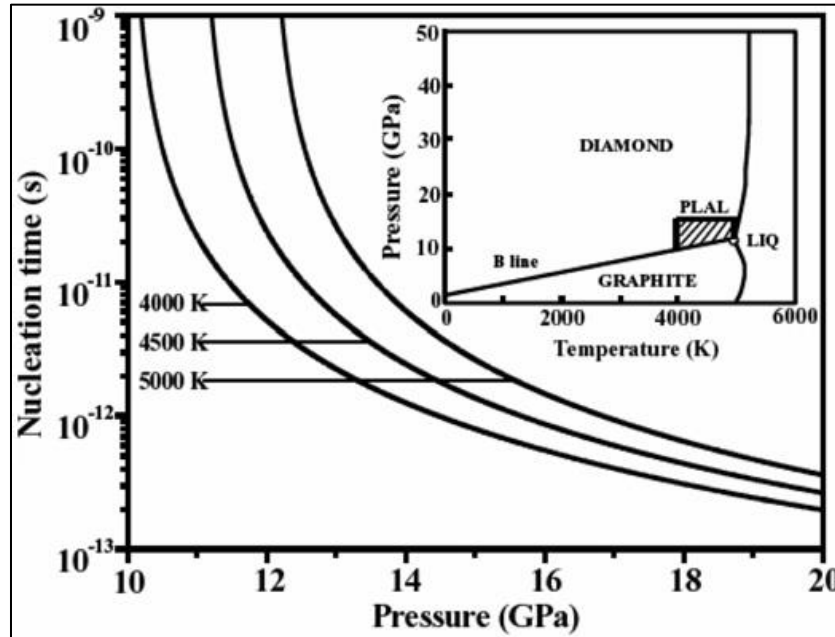


Figure 18 - Nucleation time dependence on pressure at given temperatures, for a graphite target to phase change to diamond. It is also possible to see the pressure-temperature diagram of carbon in inset [48]

2.2.6 Comparison between Femtosecond and Nanosecond laser ablation

Femtosecond pulse durations are much shorter than the typical coupling times between electron and lattice reservoirs, meaning that heat diffusion, material ejection and plasma plume formation occur significantly after the pulse interacts with the target, fully decoupling the effects. In fact, due to the short pulse duration, femtosecond pulses do not usually interact with the ejected material, as the laser induced plasma (LIP) only occurs several picoseconds after the laser energy deposition, which is the typical electron relaxation time (around 10^{-9} s). Relaxation times include the electron-to-ion energy transfer, electron heat conduction and electron-phonon coupling times [14], [24]. This means that the absorbed laser energy is confined to the initial focal volume, which improves the ablation process, without thermal processes occurring like melting, vaporization, heat propagation, etc. In the case of nanosecond pulsed laser, all these phenomena occur during the pulse duration, which means different interactions and mechanisms of ablation (mentioned above). The heated volume is mainly governed by electron photon absorption for femtosecond system, while thermal diffusion is mainly responsible in the case of nanosecond system.

Figure 19 illustrates the time scale of both femtosecond and nanosecond laser ablation processes. Figure 20 also illustrates the evolution of the ablation process, marking the difference between femtosecond and nanosecond laser systems.

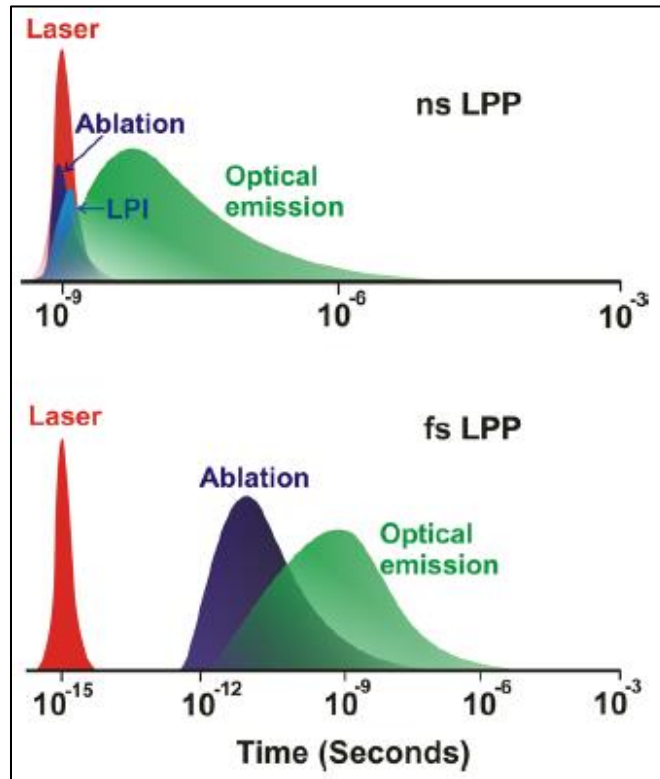


Figure 19 – Timescales for both nanosecond and femtosecond pulsed laser ablation and visible emission from the plasma [49]. Optical emission occurs after the ablation process in both cases, but in femtosecond case, the ablation occurs well after the pulse ends, while in nanosecond ablation occurs while the pulse is still irradiating the target

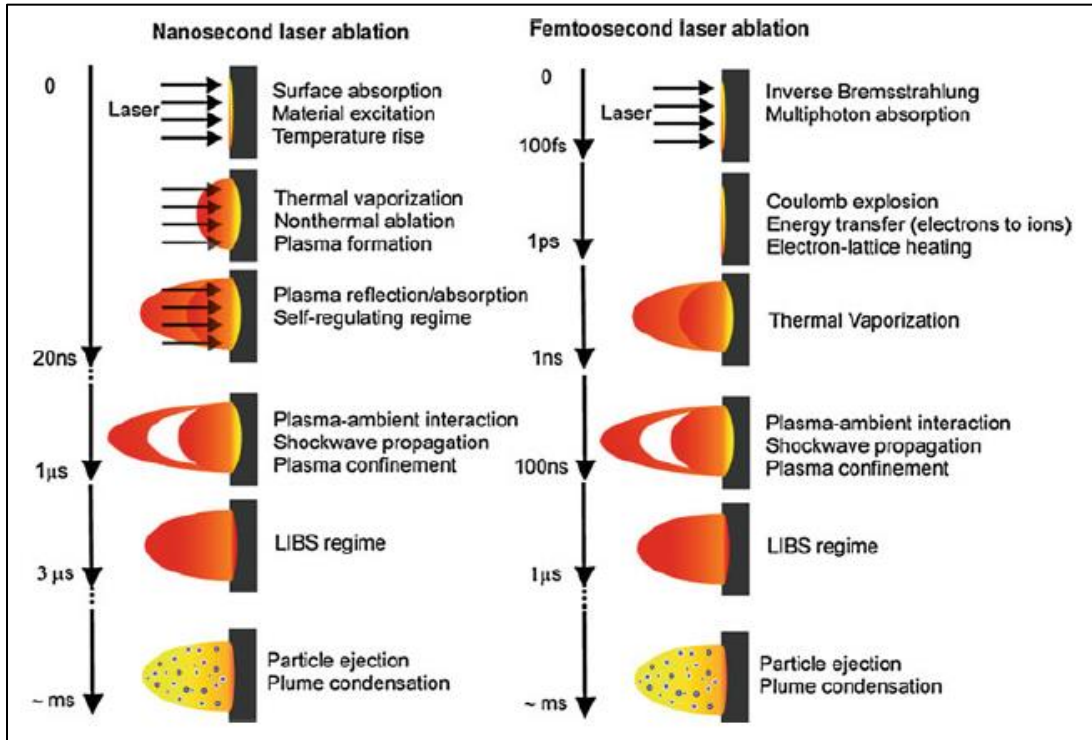


Figure 20 – Illustration of timescales of nanosecond and femtosecond laser ablation processes, during and after the respective laser pulse [24]

Due to negligible or non-existing thermal processes, the most significant contribution to femtosecond ablation comes from free electron generation. This is possible because of the nonlinear processes that occur, becoming more significant during ultrafast laser absorption, given the high peak intensities. According to [24], the major processes for laser absorption, energy transport and free electron generation are the electron impact ionization and strong electric field ionization. Before explaining these processes, it is important to say that both absorption and ablation processes differ from metals to dielectrics. In metals, electrons from the conduction band absorb photons by inverse Bremsstrahlung, and in dielectrics, if the absorbed photon does not have enough energy to overcome the band gap, then the electron will go back to the initial state, reemitting the photon [24].

During exposure to the laser, the electrons of the material will absorb photons and their energy. If a free electron receives this energy, that is equal or greater than the ionization energy of the atoms at the material surface, then this free electron can collide with a bond electron, overcoming the ionization potential barrier, turning the bonded Gd into a free one. This is called the Electron Impact Ionization (EII), and it is possible to duplicate the number of existing free electrons. After a

series of collisions, this process becomes known as the electron avalanche or optical breakdown, because of its domino type effect [24].

For higher laser intensities, from 10^{13} W·cm⁻², Strong Electric Field Ionization (SEFI) or photoionization becomes significant [24]. There are two main processes in SEFI: Multi photon Ionization (MPI) and Tunnel Ionization (TI). MPI is characterized, as the name states, by the absorption of more than one photon by an electron, before it decays to its original state, usually occurring when the photon flux is very high [24], [50]. If the combined energy of the absorbed photons is greater than the ionization potential, then the electron will be excited to the conduction band and becomes free, with kinetic energy equal to the difference between the absorbed energy and the ionization potential. This case is significant in dielectrics or semiconductors. This process dominates until approximately 10^{15} W·cm⁻², when Tunnel Ionization (TI) becomes stronger [24]. In TI, the electric field created by the laser beam changes the band structure, reducing the ionization potential barrier between valence and conduction bands, thus becoming easier to ionize electrons from the sample. Because the intensity for TI is 10^{15} W·cm⁻², higher than the typical used in fs based ablation systems, this process is not considered to be significant [24]. L. V. Keldysh [51] studied the theory of ionization of atoms in the presence of a strong laser field. He introduced a parameter γ that separates the regimes when MPI and TI occur, defined as:

$$\gamma = \frac{\omega}{F} \sqrt{2E} \quad (1)$$

where ω is the laser frequency, F the laser electric field, and E the ionization potential of the atom. It is stated that if $\gamma < 1$, tunnel ionization prevails, and if $\gamma > 1$, multi photon ionization occurs.

Kaiser et al. investigated the contribution of SEFI and EII to the free electron density [52] using a 500 nm laser pulse, with an electric field of 150 MV·cm⁻¹ irradiated on a SiO₂ target. The varying parameter was the pulse length, going from 25 fs to 200 fs. *Figure 21* illustrates the results obtained. From the image, it can be seen that electron impact ionization contribution is very low comparing to strong electric field ionization. The rate of SEFI is directly connected to the laser electric field, so it is expected that for a step-like pulse the ionization from this process increases linearly with time. As the pulse length increases, so does the influence of the impact ionization, because there are more electrons with sufficient energy to perform ionization. Each impacted electron with enough energy to ionize shifts a bound electron to the conduction band, doubling the number of electrons in the conduction band, and so this process grows exponentially with time.

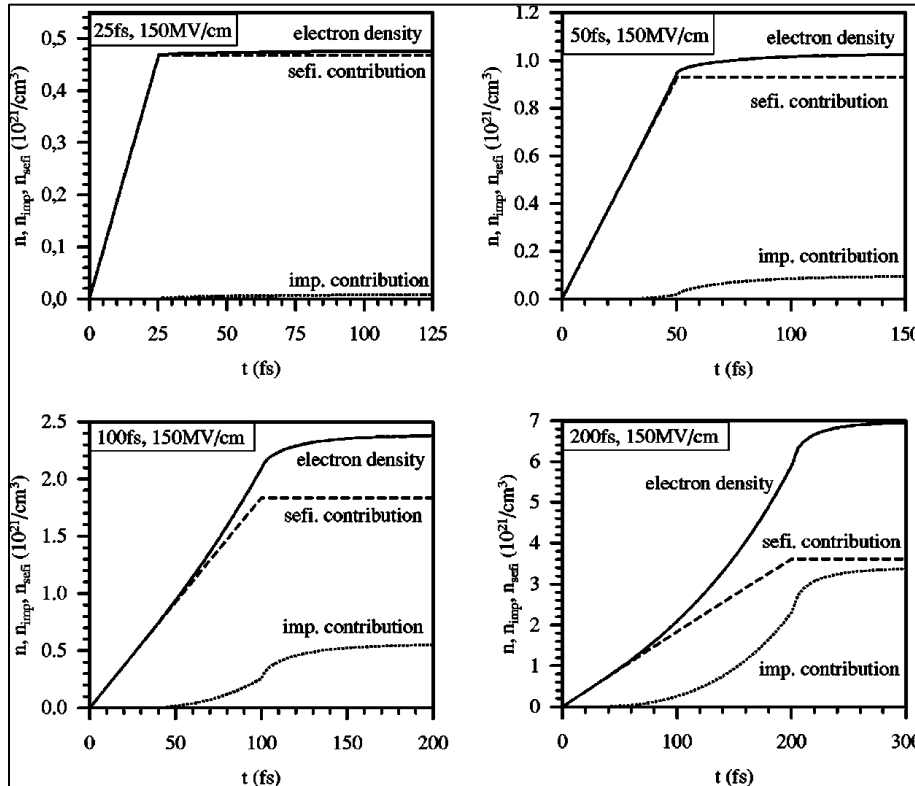


Figure 21 - Free electron time dependence for the contributing processes, SEFI and EII. A 500 nm laser pulse, with an electric field of $150 \text{ MV}\cdot\text{cm}^{-1}$, with varying pulse lengths from 25 fs to 200 fs, irradiated on a SiO_2 target [52]

Usually, femtosecond laser ablation is considered as a better ablation mechanism than nanosecond, presenting several advantages over the latter. Some of the advantages are: negligible heat effect and heat affected zone, which prevents damaging or melting the target material or even the produced NPs; the peak intensity can reach much higher values ($>10^{12} \text{ W}\cdot\text{cm}^{-2}$) than in nanosecond case ($<10^{10} \text{ W}\cdot\text{cm}^{-2}$), creating extreme conditions, like very high temperature, pressure and species density, which are favorable for the formation and even stabilization of metastable phases [14]; the initial stoichiometry remains unchanged for most of the cases during the process of ablation from bulk to nanoparticles; according to [24], [53], femtosecond pulses present higher spatial resolution than nanosecond ones. Another advantage of femtosecond laser ablation is the average size and size distribution of the produced nanoparticles, which are usually lower than nanosecond ablation produced nanoparticles. Smaller nanoparticles are desirable for some applications, such as biomedical, micromachining and medical surgery [7]-[9], [34] due to lower or none magnetic domain walls, lower saturation magnetization, etc.

One observable difference between femto- and nanosecond laser ablations is the plume morphology. Femtosecond plume is much narrower and non-spatially uniform comparing to the nanosecond one. *Figure 22* depicts such difference. The femtosecond produced plasma plume expansion has a preferable direction, normal to the surface of the target. This recoil effect may be attributed to the pressure confinement and overheating in the laser impact zone [24].

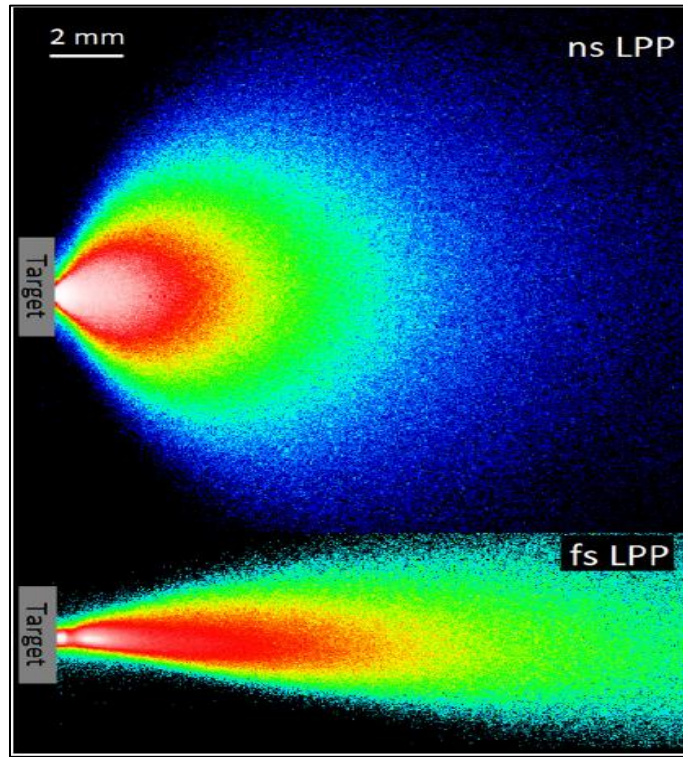


Figure 22 - Time and spectral integrated ICCD images of nanosecond and femtosecond laser-produced plasmas (LPP) under similar laser fluence conditions. The delay and integration times used for these images are 0 ns and 2 μ s [49]

Another characteristic of the femtosecond interaction is the hole morphology after the ablation. As can be seen in Figure 23, the shape of the ablated zone by femtosecond laser is clearly much more uniform and with well-defined edges. As for the crater produced by a nanosecond laser, it is much more irregular, both at surface and internal profile, that are consequence of melted and splashed material [23], [24]. According to Chichkov, the irregular profile around the hole edges is due to the recoil vapor pressure. A thermal wave propagates into the target, creating a large molten layer, which enables the removal of the target material in both liquid and vapor phases, as the vaporization process creates a recoil pressure that expels the liquid.

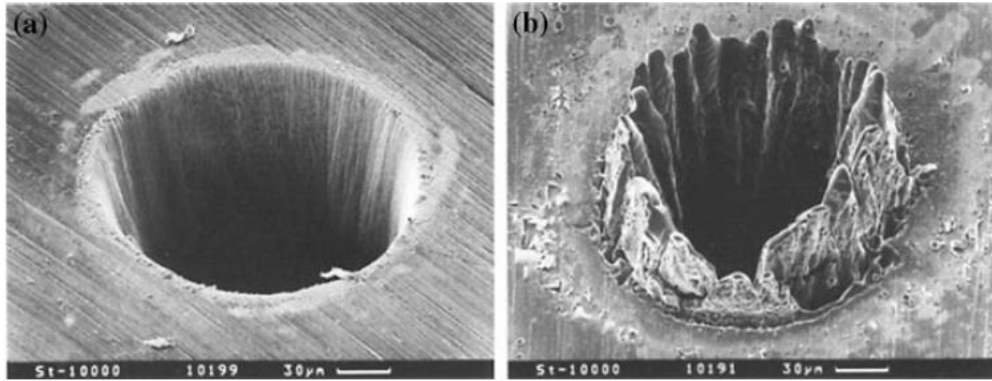


Figure 23 - Laser ablation craters in a 100 μm thick steel foil with (a) 200 fs, 780 nm and 120 μJ; and (b) 3.3 ns, 780 nm and 1 mJ laser pulses (after [23], [24])

Table 1 summarizes the main aspects of femtosecond and nanosecond processes, properties and other aspects. Notice that some of the ablation mechanisms present in *Table 1* were considered to be present in nanosecond and femtosecond, based on their respective thermal nature, as it is presented in [54].

<i>Aspect of ablation</i>	<i>Nanosecond</i>	<i>Femtosecond</i>
<i>Spallation</i>	<i>No</i>	<i>Yes</i>
<i>Fragmentation</i>	<i>Yes</i>	<i>Yes</i>
<i>Phase explosion</i>	<i>Yes</i>	<i>Yes</i>
<i>Spinodal decomposition</i>	<i>Yes</i>	<i>Yes</i>
<i>Coulomb explosion</i>	<i>Yes</i>	<i>Yes</i>
<i>Photo thermal ablation</i>	<i>Yes</i>	<i>Yes</i>

<i>Near-field enhancement ablation</i>	Yes	Yes
<i>Heat affected zones</i>	Yes	No
<i>Typical peak intensity</i>	$<10^{10} W \cdot cm^{-2}$	$>10^{12} W \cdot cm^{-2}$
<i>Spatial resolution</i>	Lower	Higher
<i>Nanoparticles size (usual)</i>	Bigger	Smaller
<i>Nanoparticles size distribution (usual)</i>	Broader	Narrower
<i>Plume morphology</i>	Uniform, non-directional	Non-uniform, directional
<i>Crater left by ablation</i>	Irregular	Regular

Table 1 – Difference between nanosecond and femtosecond systems, considering the presented properties or aspects in the table

2.2.7 Pulsed laser ablation in liquids vs. in vacuum or controlled atmosphere

The difference between PLAL and the usual PLD is that liquids offer more confinement than a gas or vacuum, and this affects thermodynamic and kinetic aspects, like higher pressures, higher temperatures, densities of species, cooling rate, average particle size, etc., inside the plasma plume created after the impact of the laser beam [7]. Concerning these aspects, lots of processes happen during ablation, including heating, melting, ejection of material and consequent chemical reactions, both with the material itself and the surrounding liquid, shock waves, plasma creation and propagation, and more [7], [14]. All these properties concerning this method are obviously dependent on laser

parameters and target characteristics. Laser parameters include radiation wavelength, pulse duration, pulse energy and repetition rate. Additionally, there is a parameter concerning the optical setup and focusing: the laser irradiation fluence that reaches the target. This parameter also plays an important role on the mechanisms responsible for the ablation itself [14], [55]-[57].

One example is presented in *Figure 24*, where Zhu and co-workers tested the ablation depth of a Si target in air and water, for the same fluence.

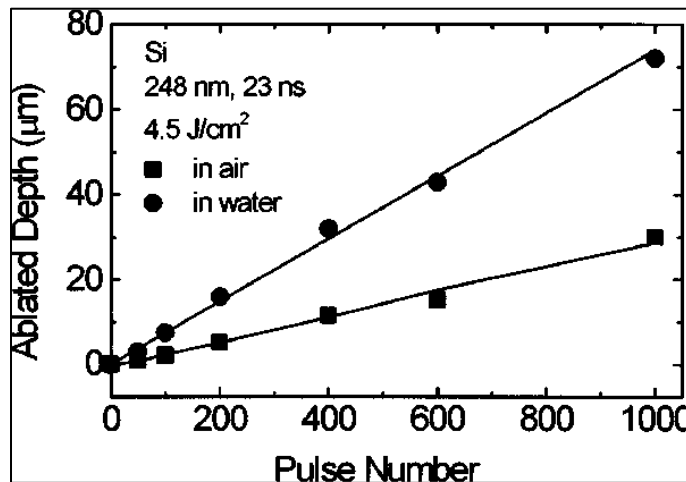


Figure 24 – Ablated depth of a Si target in air and water environments, for a laser fluence of $4.5 \text{ J}\cdot\text{cm}^{-2}$. Clearly, a linear relation exists in both cases, with the ablation rate in liquid media being higher than in air [45]

In summary, nano and femto second laser ablation in liquids offer clear opportunities for the production of new materials, in particular nanoparticles of $R_5(Si_{1-x}Ge_x)_4$.

Chapter 3 – Experimental techniques

This chapter contains the description of the experimental setups necessary for the ablation procedure, as well as the techniques used for the analysis of the resulting nanoparticles. The description of the experimental procedure is also presented.

3.1 Setup

There are two different setups used for this work, based on the lasers used for the ablation process: the KrF nanosecond laser setup and the Ti:Sapphire femtosecond laser setup. Both setups are similar, because the main difference is focused on the laser beam.

3.1.1 Nanosecond KrF Excimer PLAL setup

Our nanosecond ablation work was performed at Centro de Física da Universidade do Minho (CFUM). The laser used is a Lambda Physik LPXpro 210 pulsed excimer KrF laser with a wavelength of 248 nm and a pulse duration of 20 ns. The energy per pulse can go to a maximum of 800 mJ and the pulse repetition rate can reach 100 Hz. At the output, the laser beam cross section is $10 \times 24 \text{ mm}^2$. With a set of optical lenses and mirrors, the beam is focused in the sample. *Figure 25* illustrates the experimental ensemble with the instruments used.



Figure 25 - Nanosecond laser ablation setup. The purple line illustrates the optical beam path. The focal distance of the lens, before the mirror (beam splitter), is of 50 cm.

3.1.2 Femtosecond Ti:Sapphire PLAL setup

The femtosecond ablation took place in Femtolab, at Instituto da Física dos Materiais da Universidade do Porto (IFIMUP), in Faculdade de Ciências da Universidade do Porto (FCUP). We used a Ti:sapphire laser, model FemtoPower Compact PRO CEP, with central wavelength of 800 nm, pulse duration of ~30 fs, repetition rate of 1 kHz. At the output, the energy per pulse is 1 mJ. The beam cross section is approximately of 1,77 cm² prior to the incidence in the water where the target is fixed. *Figure 26* shows the setup used for the ablation process.

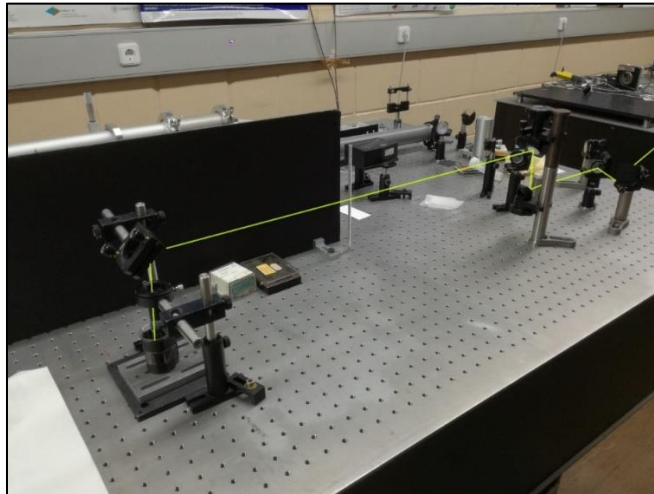


Figure 26 - Femtosecond laser ablation setup. The yellow line represents the beam optical path. The final lens focal distance is 100 mm.

3.2 Experimental techniques

Several techniques were used to characterize the produced nanoparticles, like Scanning Electron Microscopy (SEM) (and its modules, e.g. Energy Dispersion Spectroscopy (EDS)) to study the morphology of the particles, X-Ray Diffraction (XRD) pattern to study the crystallographic structure and Vibrating Sample Magnetometer (VSM) to investigate their magnetic properties. They will be briefly introduced in this section.

3.2.1 Scanning electron microscopy (SEM)

SEM (scanning electron microscopy) is a technique used for many applications, including: mapping a sample surface structure, average elemental composition, elemental composition thickness, crystal structure, etc, depending on the signal type [4].

The setup consists of an electron gun producing a high energy electron beam (20-30kV). This beam is going to be accelerated to gain more energy and then be focused by an electromagnetic optical system, composed of magnetic lenses (or condenser lens), into a small target spot on the sample surface. Using a set of deflection coils, one can move the spot location on the sample surface, allowing to map the surface and construct an image of it. A more detailed setup is shown in *Figure 27*.

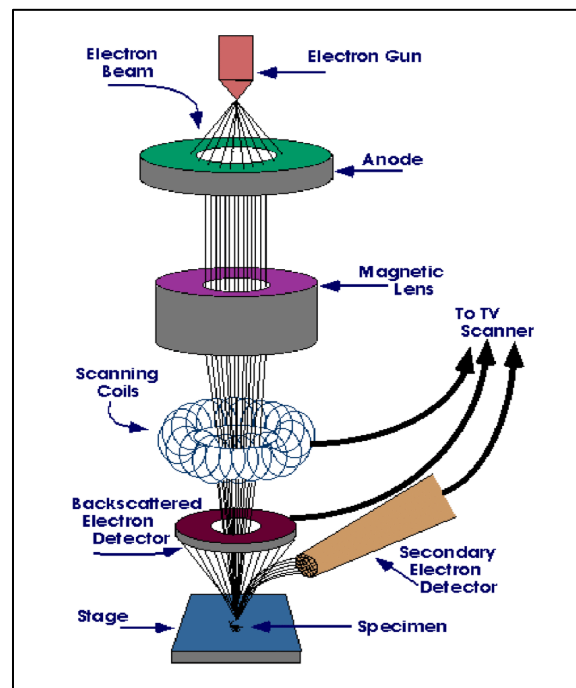


Figure 27 - Scanning Electron Microscopy (SEM) setup. The electron beam is accelerated in the anode, and then focused using magnetic lenses. The last path is through the scanning coils, where the beam is deflected horizontally and vertically, thus scanning the entire sample surface [58]

There are many different interactions when the electron beam hits the target surface. These interactions involve particles and electromagnetic radiation released by the sample, and usually happen in the near surface region. The final image comes from the detection of 2 types of particles resulting from these interactions: secondary electrons and backscattered electrons [4].

Secondary electrons (SE) originate from inelastic collisions between the incident beam and electrons on the conduction band in metals and valence electrons in insulators and semiconductors. Their interaction usually occurs in the surface or near surface region. The SE are captured by a Faraday cage, where they are accelerated, emitting light. Their intensity is related to the depth where the respective interaction occurs, so one can construct a 3D image of the topography of the sample surface, with lateral resolution of some nanometers (~50 nm).

Backscattered electrons (BSE) result from elastic collisions with electrons or nuclei of atoms of the sample. The electrons resulting from this interaction are the original electrons from the beam, only back-scattered by the atoms in the sample under study. Their interaction occurs at a greater depth than the secondary electrons. The intensity backscattered electrons is related to the atomic number of the atom that the electrons from beam encounter, bringing contrast to the image. Typically, the brighter a spot is, the larger the scatterer atomic number [4]. This is useful to distinguish impurities in the sample, or even to detect different crystallographic phases when their electronic density differs considerably. *Figure 28* depicts an illustration of the many interactions between an e-beam along the sample depth.

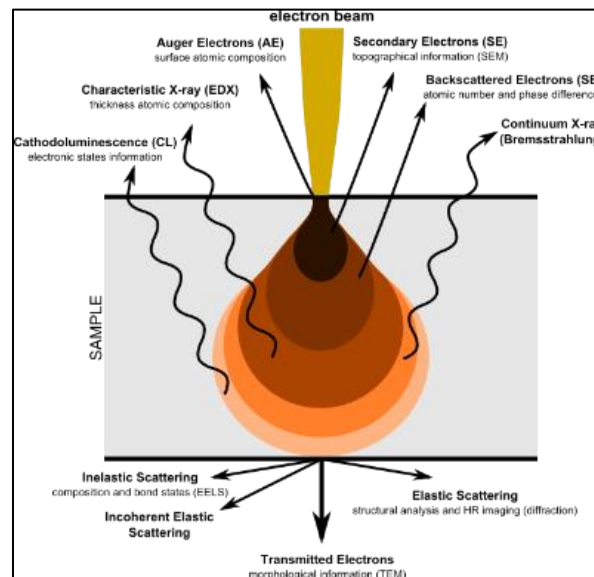


Figure 28 - Electron interaction along sample depth [59]

Samples to be examined in SEM must fulfill the following requirements: they must be good electric conductors, to not accumulate charge on the surface, thus interfering with the electron beam (this requirement is nowadays not so strict anymore in the so-called environmental SEMs); stable in

moderate/high vacuum needed for the e-beam; and thermodynamically stable in order to be able to sustain the beam effects.

3.2.1.1 Scanning Transmission Electron Microscopy (STEM)

STEM (Scanning transmission electron microscopy) is a mode of SEM, where the image is constructed using transmitted electrons. The main difference is that instead of analyzing the surface and/or near surface of the target sample, one “sees” the interior of the sample, what is its composition, layer thicknesses, crystallographic structure, and other aspects of the sample.

The setup is similar to the one of SEM and is presented in *Figure 29*. The only difference is that the electrons that pass through the sample are the ones to be collected and analyzed, which bring information of the interior composition of the sample. Then two types of images are formed: annular dark-field (ADF) and bright field (BF) images [60]. The contrast brought up by these images is what permits to understand the inner composition of the sample. Before reaching the sample, the beam is focused on a tiny spot on the sample surface by using an optical system composed of lenses, deflection coils, and objectives. There are other differences between SEM and STEM. Among them, the diameter of the beam is larger in STEM; the depth of field is lower; the acceleration voltage is much higher in STEM (100-300kV) than in SEM (~15kV), because electrons must have sufficient energy to pass through the entire sample; the sample does not need to be as thin as in SEM, so sample preparation is much easier; etc.

For this work, the sample preparation involves dropping a solution of the sample in a carbon coated copper grid that goes in STEM. Then, with the help of a STEM professional, sections of the grid are analyzed until the best images are found. STEM model used is a FEI Quanta 400FEG ESEM / EDAX Genesis X4M, that is present at Centro de Materiais da Universidade do Porto (CEMUP).

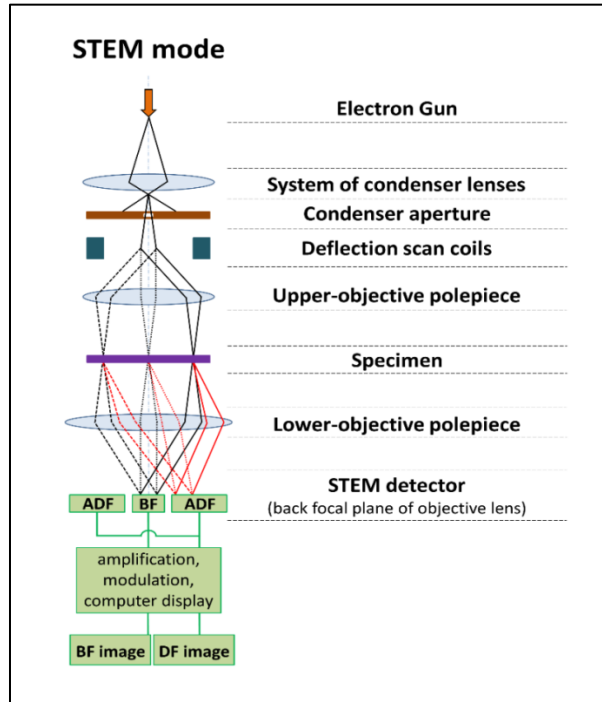


Figure 29 - STEM setup. As in SEM, the electron beam path is similar, with condenser lenses and deflection coils to scan the target. After the beam passes through the sample, is collected and then analyzed to form Annular dark-field (ADF) and Bright field (BF) imaging [61]

3.2.1.2 Energy Dispersive (X-Ray) Spectroscopy (ED(X)S)

To characterize a sample, we also need to know what are its components. EDXS is a technique that allows to estimate the chemical composition and proportion of the elements in the sample. Usually, it can be incorporated in a previous SEM setup [4]. This setup is represented in *Figure 30*. This was the device used in our work, whose model is FEG ESEM/EDS/EBSD: FEI Quanta 400 FEG + EDAX Genesis X4M.



Figure 30 - SEM and EDX setup

This technique is based in the interaction with the electron beam like in SEM, more specifically in the resulting radiation emitted as X-rays. It occurs when an electron from the outer shells occupies a hole on an inner shell, left empty by one electron that was extracted (Auger electrons) due to the energy transferred by the incident electrons. Different elements have different energy between core shells, and so by this method we can identify the chemical composition and proportion of atomic species in the present sample, by detecting the energy and intensity, respectively, of the emitted X-Rays and comparing to already known radiation spectra. An illustration is represented in *Figure 31*.

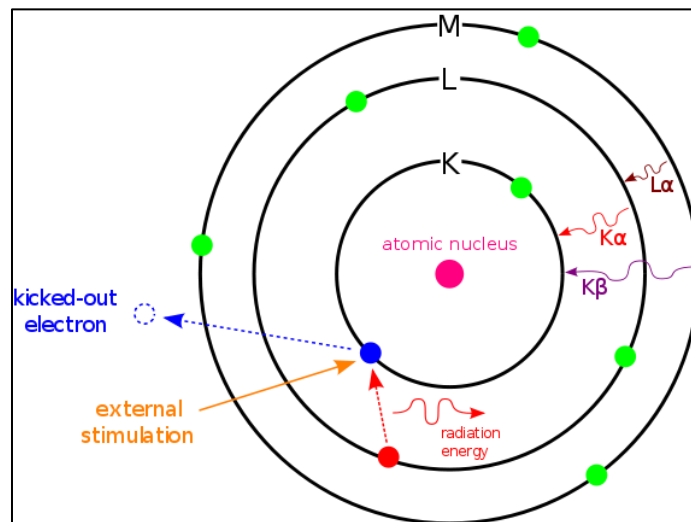


Figure 31 - Illustration of Auger electrons and EDX spectroscopy principle [62]

3.2.2 X-Ray Diffraction (XRD)

XRD (X-Ray Diffraction) is a technique used to study the crystallographic structure of materials. The information retrieved from this technique can show many crystallographic aspects of the sample being analyzed: the percentage of different structural phases, the Bravais lattice (all its parameters, such as unit cell lengths and angles), electronic distribution, symmetry group, etc.

In simple terms, X-Ray Diffraction is based on the Bragg law, which states that a crystal, when irradiated with X-Ray light, will create a diffraction pattern, that strongly depends on the crystalline structure. The atomic structure of crystals is such that the atomic distance between atoms in a unit cell (fundamental repeatable structure that characterizes a crystal) is in the order of angstroms (Å). If we use X-Rays, whose wavelength is of the same order of magnitude, then the crystal behaves as a diffraction grid. According to Bragg, only light that adds coherently will create the diffraction pattern. If we think of a crystal as a set of planes of atoms, oriented in a certain direction, then only rays of incident light that have a difference in optical path equal to multiples of its wavelength will add coherently, as can be seen on the scheme of *Figure 32*. This different optical path for incident light depends on the angle of incidence of radiation to the normal of the planes, its wavelength and the distance between families of planes. More thoroughly, Bragg's law is represented by the following equation:

$$2d_{hkl}\sin(\theta) = \lambda \quad (2)$$

where d_{hkl} is the distance between planes normal to the vector represented by hkl (the Miller indices) [63], which are coefficients of the primary vectors of the unit cell; θ is the angle between the incident light and the normal to the planes; and λ the wavelength of light (n is an integer). *Figure 32* depicts the process of diffraction.

The XRD setup is well known where the X-ray beam is passes through different slits before hitting the sample. Then the reflected beam will pass through 2 more slits, until it reaches the detector. The slits are used to control/reduce the flow of light and its divergence, either to focus more in the center of the sample and avoid reflections from the sample holder, or to reduce the amount of light that reaches the detector to avoid damage.

Our work was done using powders of $Gd_5(Si_{1-x}Ge_x)_4$. The setup allowed two configurations to be used to analyze the samples: Bragg-Brentano or Parallel Beam. *Figure 33* and *Figure 34* illustrate each of these geometries.

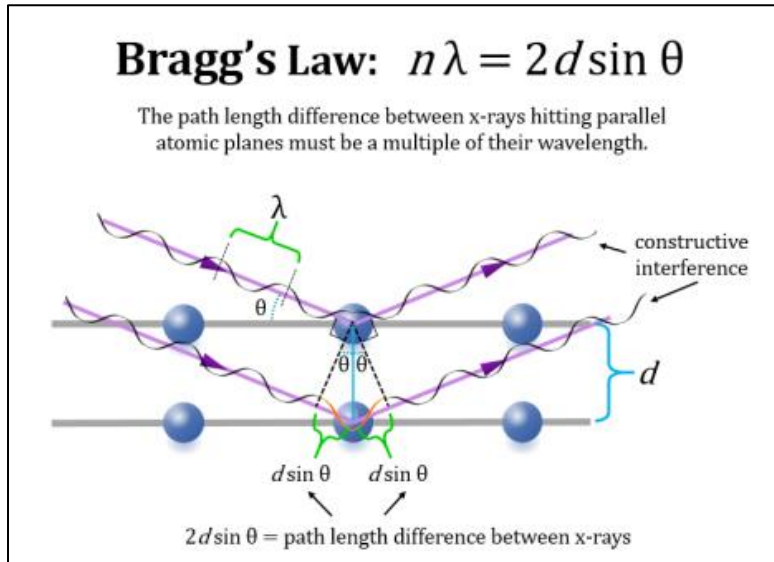


Figure 32 - Bragg law, and X-Ray diffraction [64]

With Bragg-Brentano geometry it is possible to acquire high resolution and high intensity data. The beam is divergent, and can cover the entire sample, therefore there are more data received, and higher intensities in each measurement. The sample should be however very flat, to allow a balanced trade-off between intensity and accuracy with this method.

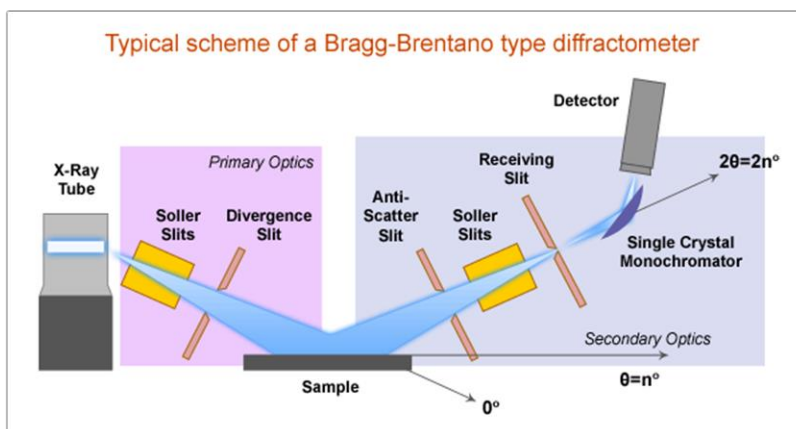


Figure 33 - Bragg-Brentano geometry [65]

With Parallel Beam geometry, the intensity measured is lower. However, PB geometry can be used no matter the sample shape. Therefore, it is very good to analyze grains, powders,

nanoparticles, thin films, etc. Because the beam is collimated, we know that for each angle pair of the X-ray source/detector, only contributions from the same families of planes are registered. Additionally when the sample holder is highly crystalline we can discard the sample holder contribution by simply tilting it in such a way that the Bragg equation is never fulfilled.

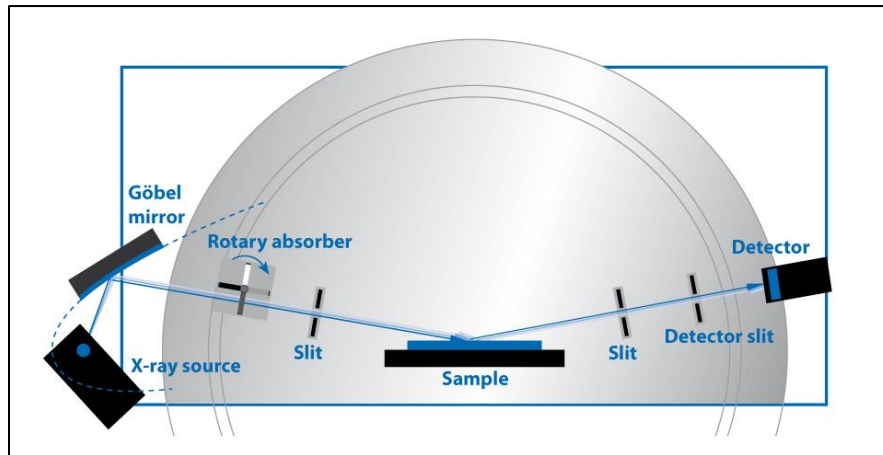


Figure 34 - Parallel beam geometry [66]

To prepare the sample, we follow a similar procedure as in the STEM. However, this time a solution is dropped in the silicon wafer, until it dries. Then we proceed with the measurements, using the appropriate geometry.

3.2.3 Vibrating sample magnetometer (VSM)

Vibrating Sample Magnetometer (VSM) is the most used tool for determining and measuring magnetic properties of magnetic materials as a function of magnetic field, temperature and time. One of the reasons to its preferability is due to the fact that measurements can be performed on solids, liquids, powders, single crystals, thin films, nanostructures, etc. These magnetometers are also employed because measurements can be performed over a vast range of temperatures (4 K to 1273 K), that simulate the environmental conditions to which the magnets may be exposed [63], allowing also to study several magnetic/structural phase transitions.

When a material is placed within a uniform magnetic field H , a magnetic moment \mathbf{m} will be induced in the sample. In a VSM, the sample is placed within carefully placed sensing coils, and a sinusoidal motion is applied to the sample, which means that the sample vibrates. The resulting magnetic flux change induces a voltage in the sensing coils that is theoretically proportional to the

sample magnetic moment. Usually, the magnetic field is generated by electromagnets, or from superconducting magnets. Variable temperatures from cryogenic to high temperatures ones may be achieved using either cryostats or furnace assemblies, respectively.

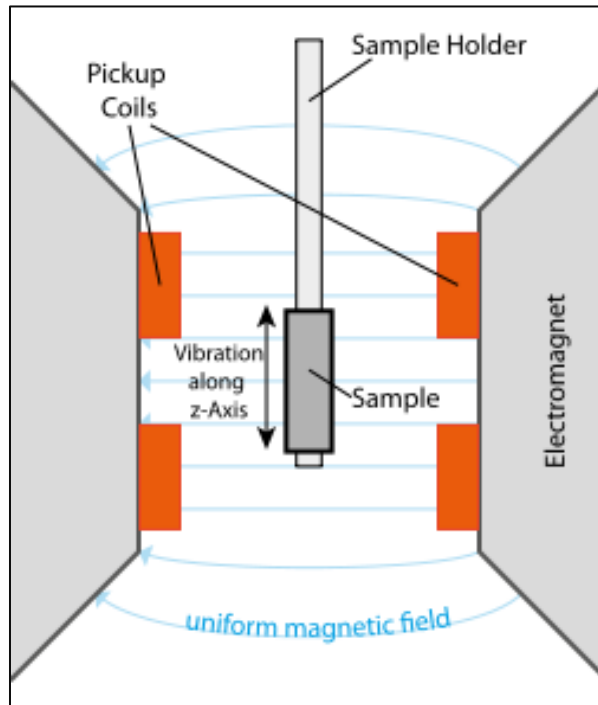


Figure 35 – VSM setup scheme [67]

3.3 Experimental procedure

The experimental procedure consists of the following steps:

1. Before the laser ablation session, the surface of the bulk target must be polished, in order to achieve a uniform ablation, with no irregularities;
2. In the ablation session, the recipient must be washed with acetone, followed by a second wash with deionized water;
3. The recipient is filled with the desired amount of deionized water;
4. The laser parameters are measured, like the power of the laser beam (using a photometer), laser frequency, laser fluence is estimated, etc;
5. The laser ablation starts. In some cases, usually in the longer ablations, the bulk target was moved in order to change the spot that was being ablated, in order to try to have more material ablated;
6. After the ablation, the solution was stored in small recipients (Eppendorf). Later, this solution was used in a centrifuge, for the purpose of separating the smaller nanoparticles, while being partially substituted with acetone at each centrifugation. After 4 steps, we had the smaller nanoparticles in acetone solution, and it was left to dry/evaporate (the acetone), so at the end all that was left was the remaining powder;
7. The last step depends on the technique used in the powder. If it was to be used in SEM, the solution (while with acetone) was centrifuged and the bottom of the solution was collected and deposited on the copper grid to be analyzed; for XRD measurements, the procedure was the same, but instead of a copper grid, we had the sample holder, where the solution was deposited and left to dry.

Chapter 4 – Results and discussion

4.1 Targets structural and magnetic characterization

Characterization of bulk targets of $Gd_5Si_2Ge_2$ and $Gd_5Si_{2.2}Ge_{1.8}$ were performed by refining XRD pattern data. The resulted fitted curves are presented in Figure 36 and Figure 37 and the lattice parameters of main phases are summarized on Table 2. For $Gd_5Si_2Ge_2$ bulk target, the M structure is the majority phase corresponding to the fraction of 81.63 %, with the unit cell volume of 867 nm^3 in fine agreement with previous reports [2], [68], [69]. For $Gd_5Si_{2.2}Ge_{1.8}$, additionally to the mixture of M and O(I) phases, there is the formation of an eutectic 5:3-phase with a hexagonal symmetry (P63mcm space group) formed during the fast cooling after arc melting, commonly observed for this family of compounds [68] (results in Table 2). However, because its presence is below 5%, we will prepare the nanoparticles expecting that such phase will vanish due to the laser-target interactions.

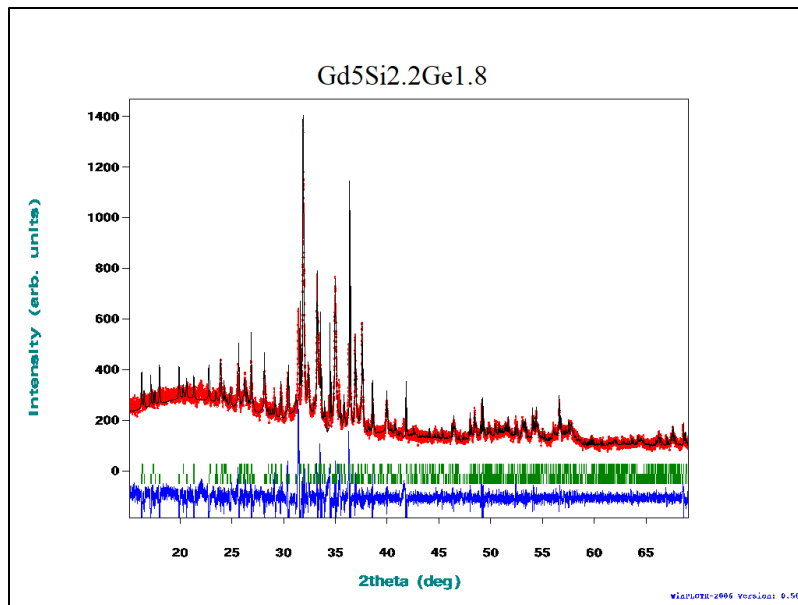


Figure 36 - Rietveld refinement of the XRD pattern of the $Gd_5Si_{2.2}Ge_{1.8}$ bulk target

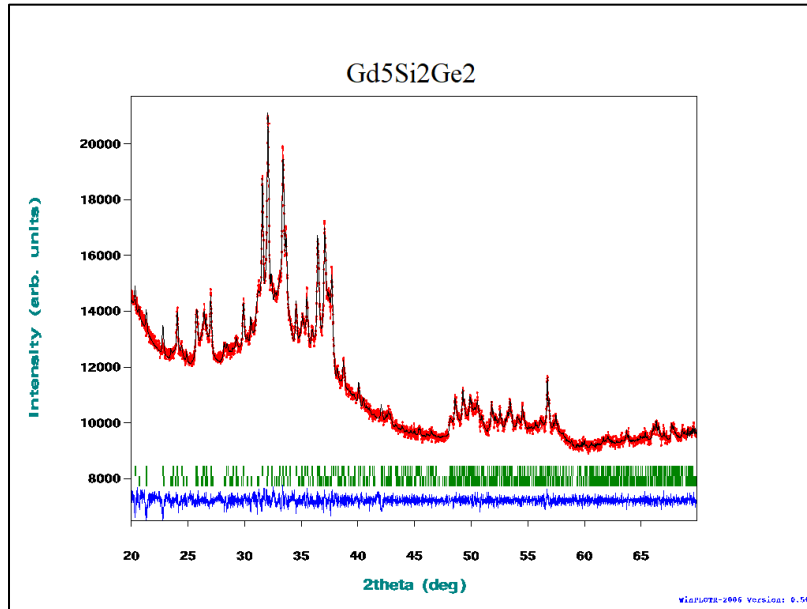


Figure 37 – Rietveld refinement of the XRD pattern for the $Gd_5Si_2Ge_2$ bulk target

Sample	Space Group	R_p	R_{wp}	R_{exp}	Chi2	a (nm)	b (nm)	c (nm)	Percentage (%)	Unit cell volume (nm^3)
$Gd_5Si_2Ge_2$	$P112_1/a$	28.9	22.4	17.94	1.56	7.584326	14.800569	7.780065	81.63	872.001
	$Pnma$	28.9	22.4	17.94	1.56	7.514549	14.787831	7.802397	18.37	867.033
$Gd_5Si_{2.2}Ge_{1.8}$	$P112_1/a$	53	48	31.35	2.34	7.439631	14.848904	7.804476	48.77	870.72
	$Pnma$	53	48	31.35	2.34	7.558489	14.812573	7.792132	45.66	872.4
	5:3	53	48	31.35	2.34	8.837170	8.837170	3.361655	5.57	430.26

Table 2 - Space group and refinement parameters of $Gd_5Si_2Ge_2$ and $Gd_5Si_{2.2}Ge_{1.8}$. Parameters a, b and c are unit cell lengths in nm

Due to the strong coupling between structural and magnetic properties of $Gd_5(Si,Ge)_4$ family compounds, the confirmation on the quality of the produced target samples was performed through magnetic measurements. The magnetization as a function of temperature (M-T) curves obtained on

cooling and heating are presented in *Figure 38* and *Figure 39* for $Gd_5Si_2Ge_2$ and $Gd_5Si_{2.2}Ge_{1.8}$, respectively, with their indicated Curie temperatures confirming the XRD analysis [1], [6], [70]. Furthermore, the saturation magnetization of 205 emu/g and 154 emu/g for both compositions are in agreement with the ~ 220 emu/g for these materials. In particular, due to the presence of 5:3-phases on the $Gd_5Si_{2.2}Ge_{1.8}$ bulk sample, there is a loss on saturation since this phase presents a Néel temperature around 50 K.

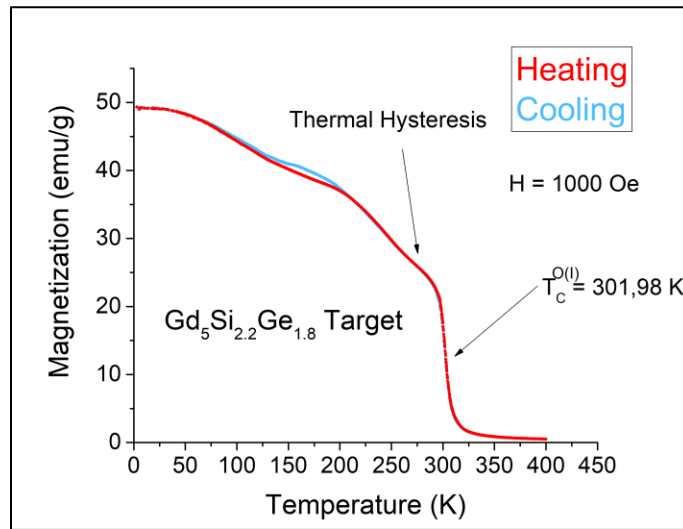


Figure 38 – $Gd_5Si_{2.2}Ge_{1.8}$ Magnetization dependence on temperature, for a fixed value of the magnetic field, for the cooling and heating curves

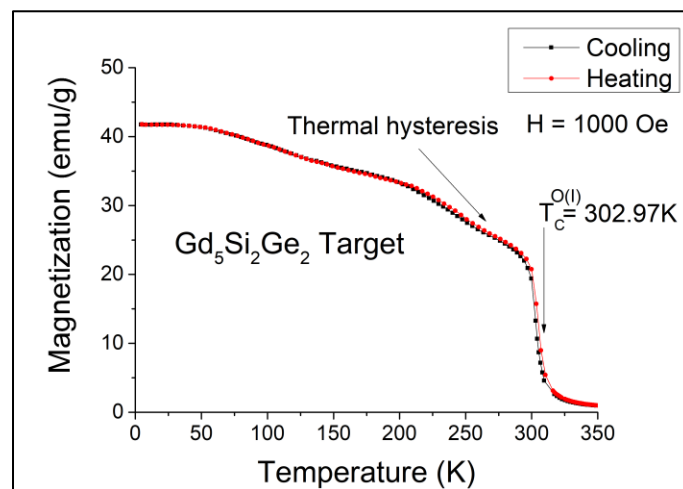


Figure 39 - $Gd_5Si_2Ge_2$ Magnetization dependence on temperature, for a fixed value of the magnetic field, for the cooling and heating curves.

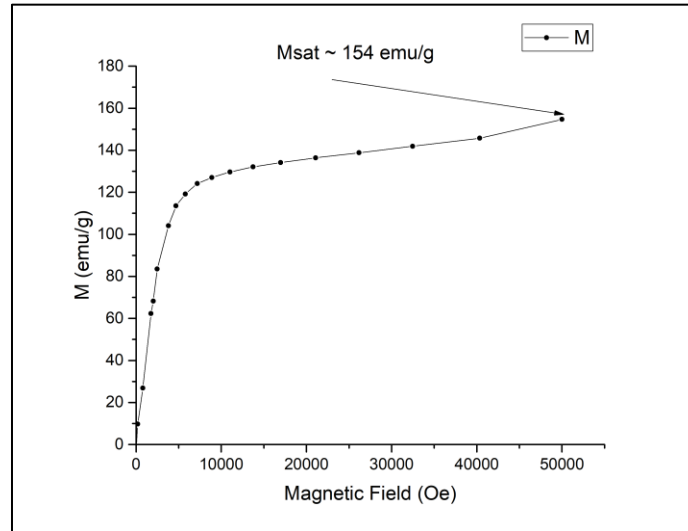


Figure 40 - $Gd_5Si_{2.2}Ge_{1.8}$ magnetization dependence on magnetic field, for a fixed value of temperature of 5K.

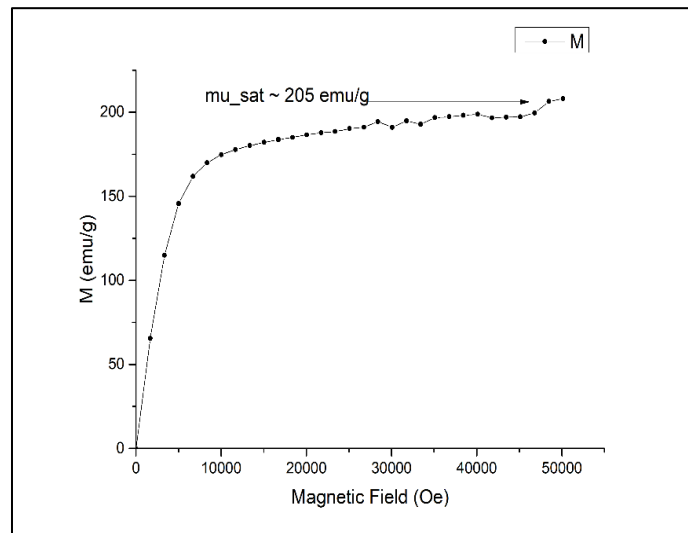


Figure 41 - $Gd_5Si_2Ge_2$ magnetization dependence on magnetic field, for a fixed value of temperature of 5K.

This initial analysis is of great importance for the nanoparticles production through laser ablation processes since the bulk characteristics will be used to understand the nanoparticles behavior.

4.2 $Gd_5(Si_xGe_{1-x})_4$ and Ni nanoparticles

4.2.1 Morphological and chemical characterization

Previously to the $Gd_5(Si_xGe_{1-x})_4$ production using laser ablation in liquids the assembled set-up was tested by using a Ni target.

$Gd_5(Si_xGe_{1-x})_4$ and Ni nanoparticles were analyzed in SEM and when possible in EDS. This section presents the results obtained for the produced nanoparticles, such as average size and size distributions of the fabricated nanoparticles.

Nanoparticles produced by nanosecond laser

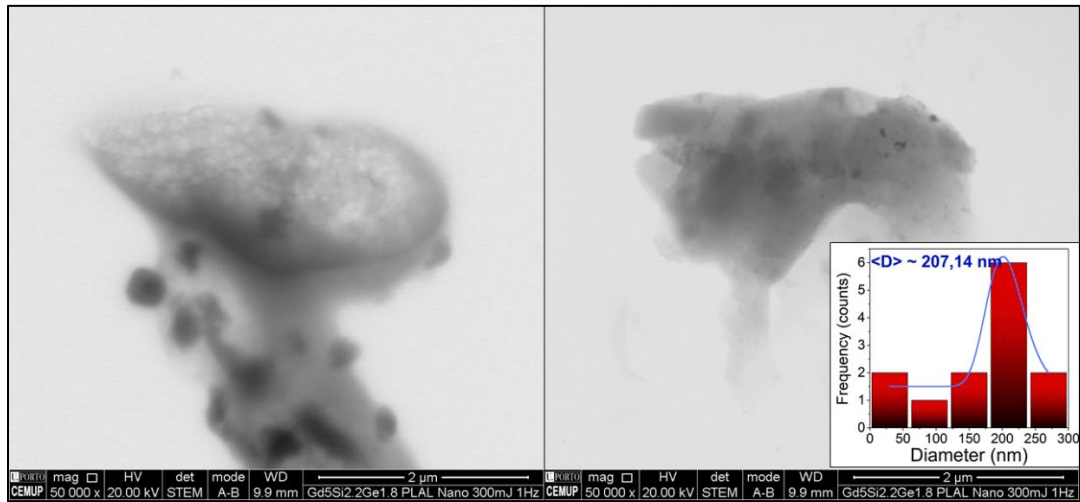


Figure 42 - SEM images of the $Gd_5Si_{2.2}Ge_{1.8}$ sample, with laser parameters of 300 mJ energy per pulse and 1 Hz frequency rate, and ablation time of 20 minutes. (inset) Size distribution of analyzed nanoparticles, with average diameter of approximately 207 nm

Figure 42 shows results with little statistical results, on the average size of nanoparticles, due in large part to the low ablation time. Despite ablating on two surfaces with the intention of getting more particles, the number is still very low. Another reason for the low number of particles is that the SEM analysis is also dependent on the collected particles from the prepared solution, and the ones that actually “stick” to the copper grid that is used. From *Figure 42* is also possible to notice a kind of matrix involving the nanoparticles, and is similar to the one obtained by Christine Floss [71]. This matrix may be a byproduct of the ablation, or the result of contamination

Figure 43 and Figure 44 present the remaining results for the nanosecond ablations. Figure 44 (left) indicates the presence of the matrix involving the nanoparticles, which suggests that this may be indeed a byproduct of the ablation, although this is still under research. The size distribution also follows the expected log normal distribution, as is stated by N. R. Checca [72].

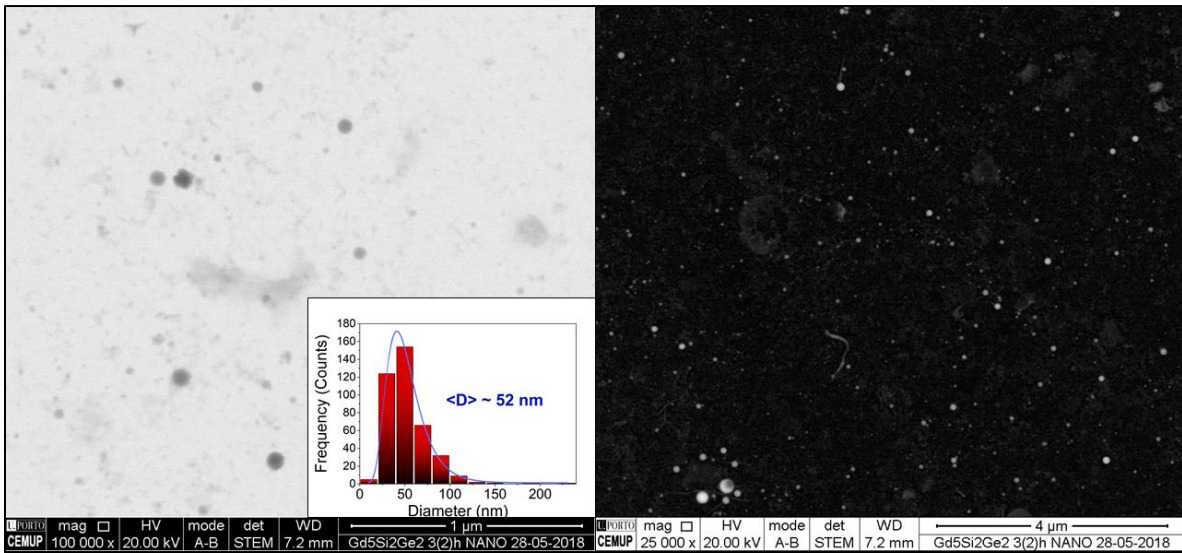


Figure 43 - SEM images of the $Gd_5Si_2Ge_2$ sample, with laser parameters of 450 mJ energy per pulse and 10 Hz frequency rate, and ablation time of 2 hours and 20 minutes. (inset) Size distribution of analyzed nanoparticles, with average diameter of approximately 52 nm

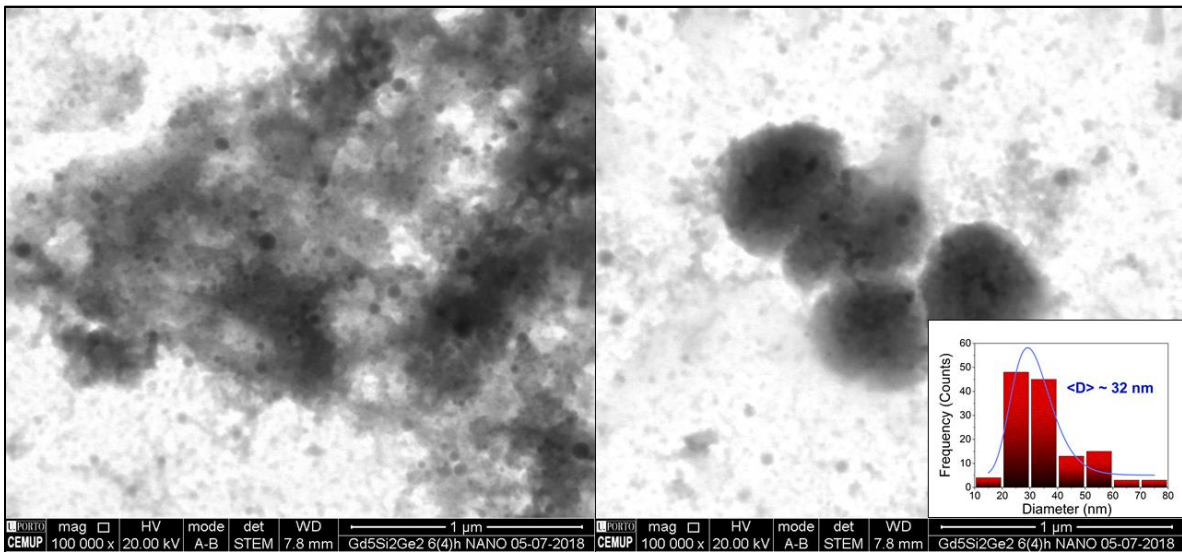


Figure 44 - SEM images of the $Gd_5Si_2Ge_2$ sample, with laser parameters of 450 mJ energy per pulse and 10 Hz frequency rate, and ablation time of 4 hours. (inset) Size distribution of analyzed nanoparticles, with average diameter of approximately 32 nm

These results also show that the average size of nanoparticles produced decreases with the ablation time. This result is expected, as it was approached previously in section 2.2.2, due to the laser pulse interacting with the ablated material in the solution, decreasing the size of the final nanoparticles.

Nanoparticles produced by femtosecond laser

Nickel

Following previous works on Ni ablation in liquid media [71,72], already mentioned, this material was chosen to test the ablation parameters before beginning with the production of $Gd_5Si_2Ge_2$ nanostructures through PLAL. Some tests were made in a similar way as in the nanosecond ablation, and even a study on the distribution of the size of nanoparticles depending on the water depth was performed.

Figure 45 (left) shows the results after SEM analysis. The ablation time was of 5 minutes, and it was taken in order to observe the impact of the laser beam on the surface of the sample. Due to the low time of ablation, a statistical analysis was not possible. *Figure 45* (right) presents a picture taken using a microscope. As can be seen, the shape and size of the area of impact confirms that there was no significant ablation, There is little thermal expansion on the area, most probably because of the low fluence used. At this stage, the fluence was not determined. However, given the parameters used, one estimates it to be around $0.33 \text{ J}\cdot\text{cm}^{-2}$.

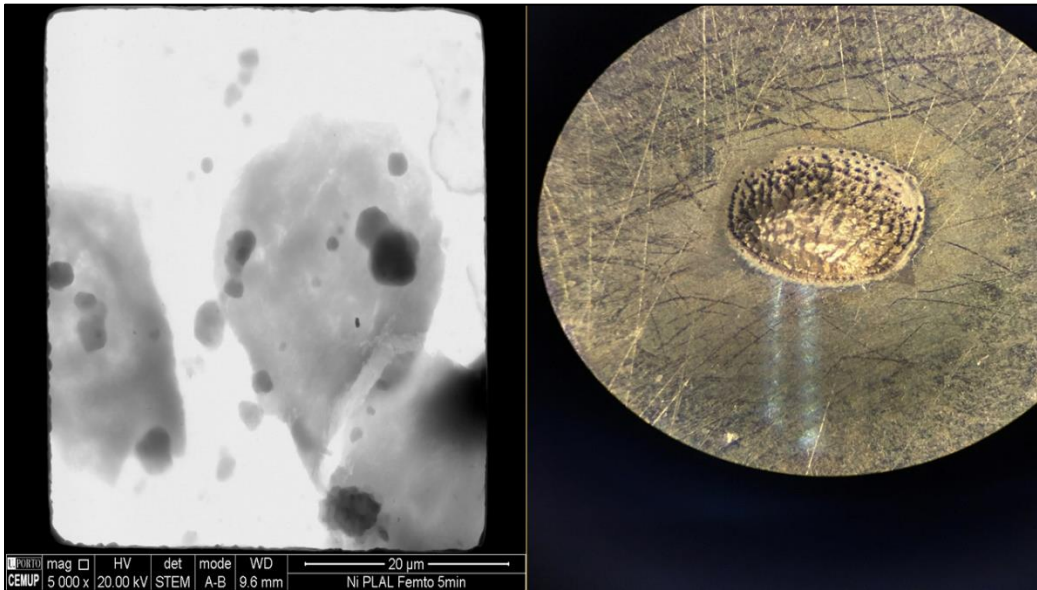


Figure 45 - (left) SEM image of the solution resultant of ablation of Nickel target for 5 minutes and (right) microscopic picture of the ablated area. There was not enough statistical data, so size distribution was not possible to obtain

Figure 46 illustrates the results of the ablation of Nickel for 10 minutes. As in the previous cases of ablation in nanosecond and femtosecond, there is a matrix involving the produced nanoparticles. As will be seen for the next results, this matrix is in most of the cases present, reinforcing the idea that it is a byproduct of the ablation of both Ni and $Gd_2Si_2Ge_2$. The inset in Figure 46 shows the result of a statistical analysis. Considering the ablation time, there is a good number of particles analyzed, and the size distribution matches a log normal one, as it was expected.

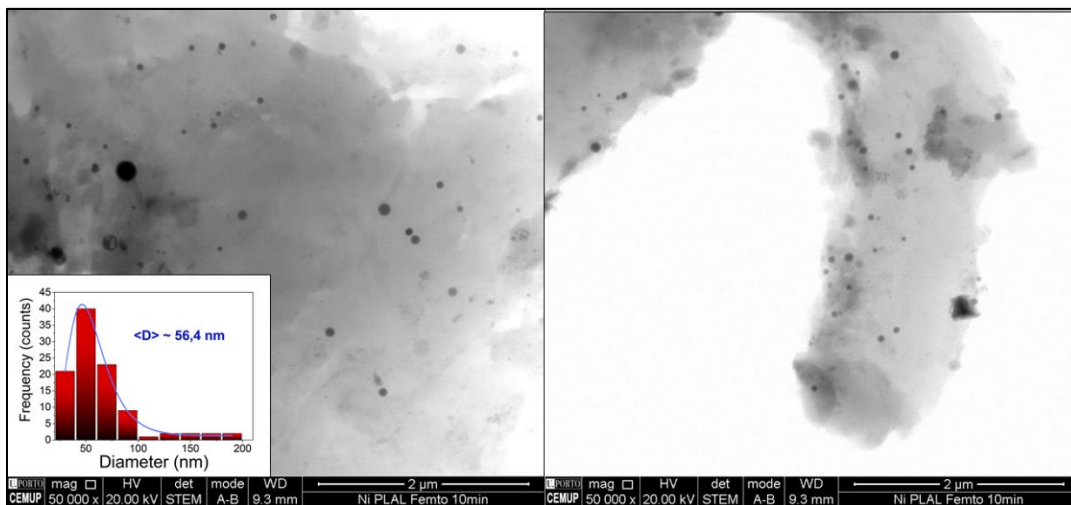


Figure 46 – SEM images of the solution resultant of ablation of Nickel target for 10 minutes. (inset) Size distribution of the analyzed particles, with average particle size of 56,4 nm

Figure 47, Figure 48 and Figure 49 present the results of the ablation of a $Gd_5Si_2Ge_2$ target during 30 minutes, collected at different depths on the solution after the ablation, respectively bottom, middle and top of the water layer. Figure 47 has low statistic compared to the other two. Besides, it also presents a much higher particle average size. We suspect from SEM images at other areas on the copper grid, that the recipient was probably contaminated at the bottom with other materials, which could explain this huge difference in average size. Figure 48 and Figure 49 show higher particle counting and a lower average particle size, as expected because they were collected at the middle and top of the water layer. Particles collected from the middle of the water layer are on average smaller than the ones collected at the top. This may seem contradictory, but if we consider that the particles were collected almost immediately after the ablation, then most of the recently produced particles were still in the middle zone and, perhaps, were collected before they could be spread in the solution. More studies need to be done in order to clarify this point. On the other hand, the particle size distribution match a log normal, as expected.

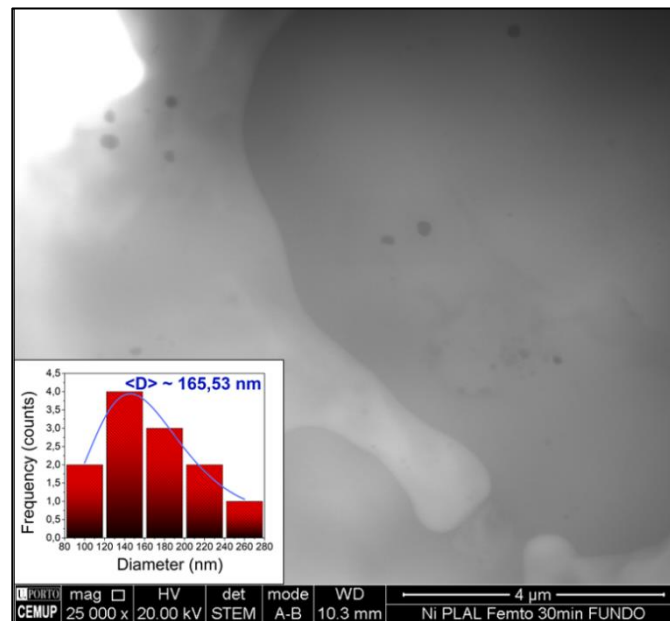


Figure 47 – SEM images of the solution resultant of ablation of Nickel target for 30 minutes and collected at the bottom of the recipient. (inset) Size distribution of the analyzed particles, with average size particle of 165 nm

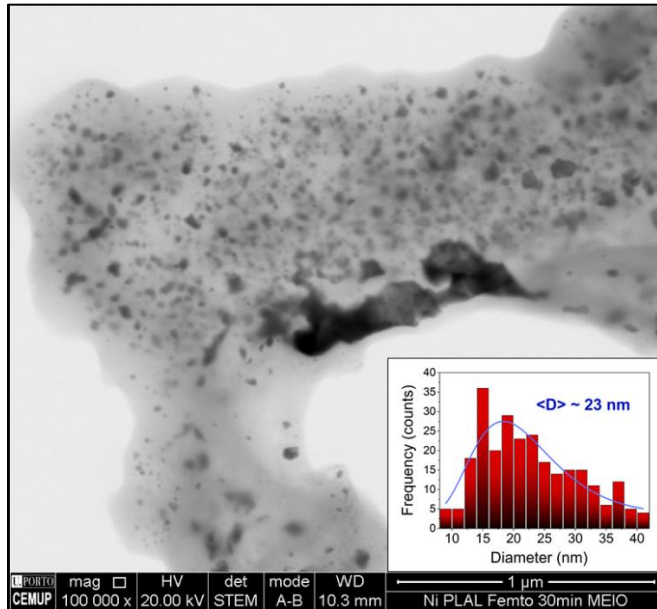


Figure 48 - SEM images of the solution resultant of ablation of Nickel target for 30 minutes and collected at the middle of the recipient. (inset) Size distribution of the analyzed particles, with average particle size of 23 nm

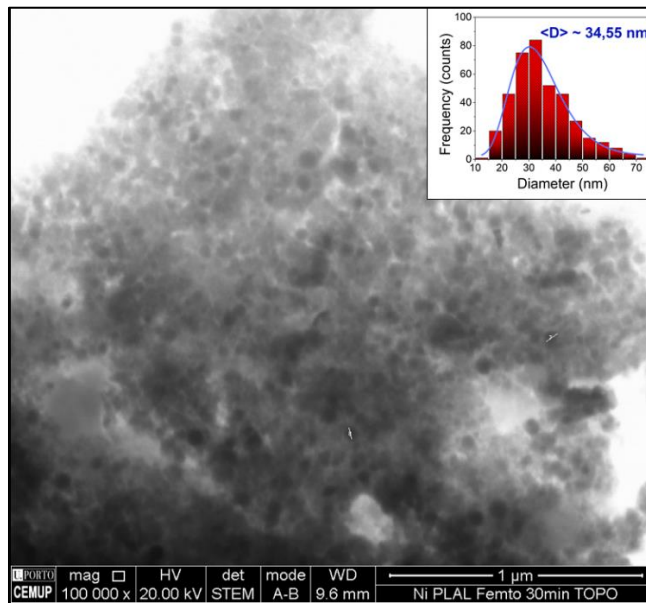


Figure 49 - SEM images of the solution resultant of ablation of Nickel target for 30 minutes and collected at the top of the recipient (near water surface). (inset) Size distribution of the analyzed particles, with average particle size of 34,5 nm

Figure 50 resumes the results obtained for the ablation of Nickel, depicting the dependence of the average particle size on the time of ablation and depth that are collected.

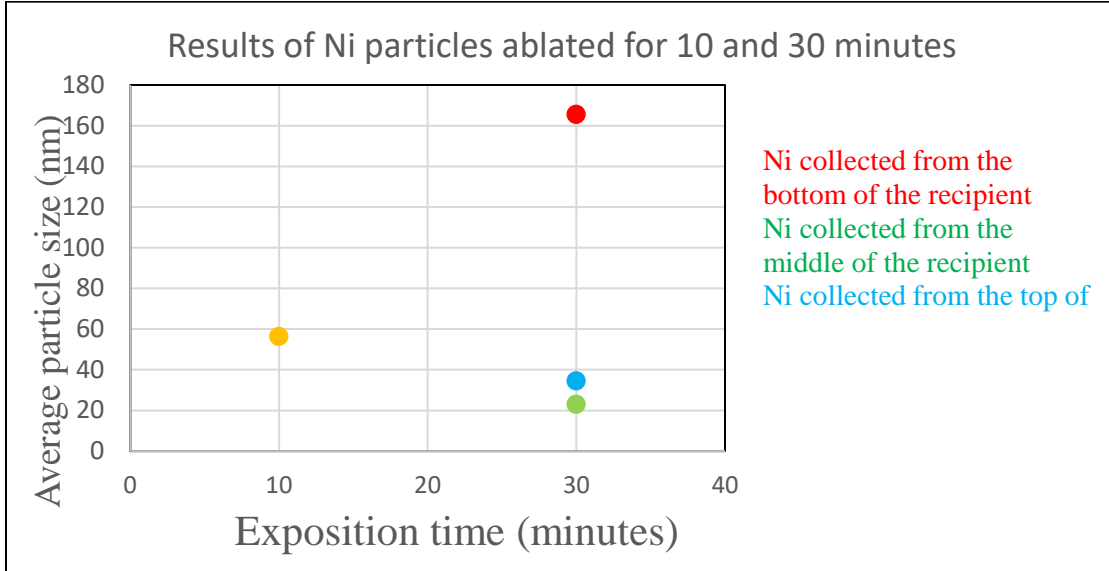


Figure 50 – Ni size dependence on time of ablation and depth of collected nanoparticles

Gd₅Si₂Ge₂

After the results of Nickel, it was time to begin working with $Gd_5Si_2Ge_2$ using this setup. The initial fluence used was set to $2 \text{ J}\cdot\text{cm}^{-2}$. *Figure 51* and *Figure 52* show the results for ablations of 40 minutes and 3 hours, respectively. The procedure is the same as for Nickel, with the only varying parameter being fluence. The fluence used in the 3 hours ablation was increased to $4 \text{ J}\cdot\text{cm}^{-2}$. The 40 minutes ablation presented an average particle size of 65 nm, while in 3 hours ablation the result was of 57 nm. The results presented in *Figure 51* have relatively low statistical results, but it is still present the tendency of lowering the average particle size with increasing time of ablation. Also, it can be seen the existence of the matrix involving the particles, being present in every sets of samples prepared in this work.

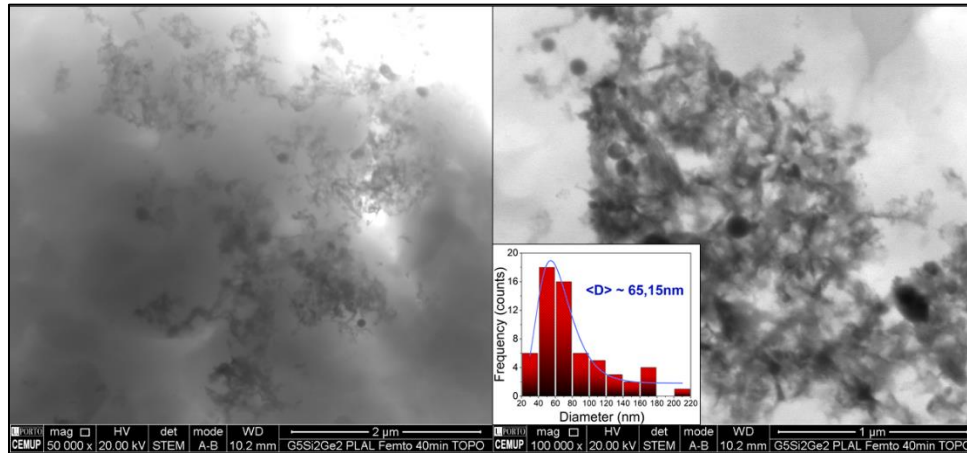


Figure 51 - SEM images of the solution resultant of ablation of $Gd_5Si_2Ge_2$ target for 40 minutes and collected at the top of the recipient (near water surface). (inset) Size distribution of the analyzed particles, with average particle size of 65 nm

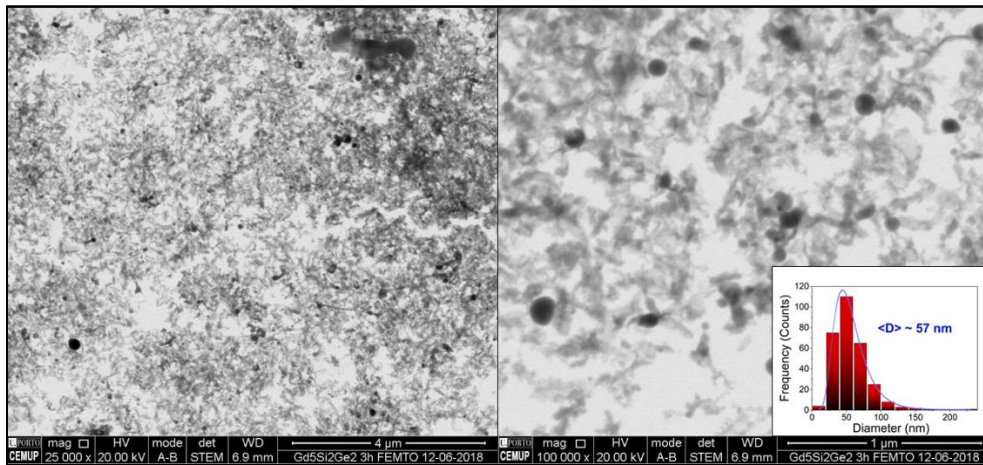


Figure 52 - SEM images of the solution resultant of ablation of $Gd_5Si_2Ge_2$ target for 3 hours and collected at the top of the recipient (near water surface). (inset) Size distribution of the analyzed particles, with average particle size of 57 nm

Figure 53 presents interesting results. The SEM image (right) shows a large agglomeration of nanoparticles, clearly proving that at some point they were created and aggregated in a single structure. N. V. Long [75] reported an aggregation of Pt nanoparticles and similar SEM results of singular aggregated nanoparticles. The average size of these nanoparticles is of 56 nm, only slightly lower than the previous ablation, despite the ablation time being of 4 hours and fluence of $2 \text{ J}\cdot\text{cm}^{-2}$.

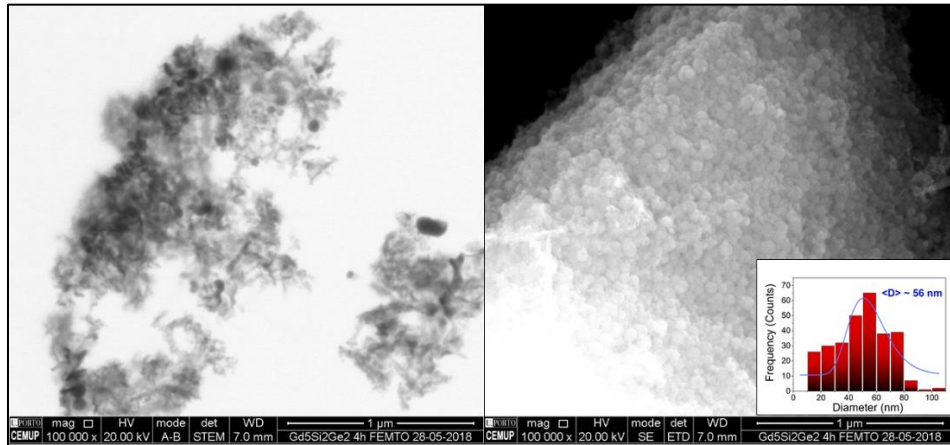


Figure 53 - SEM images of the solution resultant of ablation of $Gd_5Si_2Ge_2$ target for 4 hours. (inset) Size distribution of the analyzed particles, with average particle size of 56 nm

The final ablation on $Gd_5Si_2Ge_2$ took 8 hours, and the laser fluence used was approximately $10 \text{ J}\cdot\text{cm}^{-2}$, with an estimate error of approximately $1.5 \text{ J}\cdot\text{cm}^{-2}$, associated with the imprecision of the tenth of millimeter in the measurements of the setup. Despite the long ablation time and high fluence, the average size of the analyzed particles is of 57 nm, the same as the two previous ablations. The increase in these parameters had no apparent influence on the average size of the nanoparticles. The results are presented in *Figure 54*.

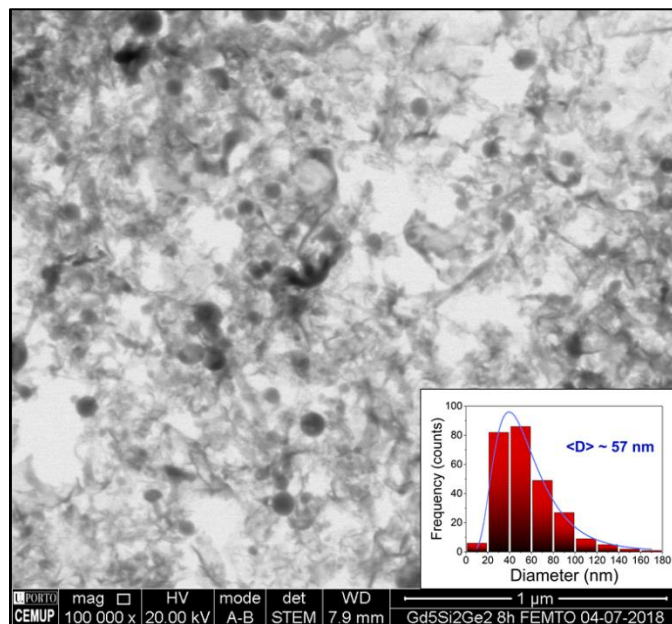


Figure 54 - SEM image of the solution resultant of ablation of $Gd_5Si_2Ge_2$ target for 8 hours. (inset) Size distribution of the analyzed particles, with average particle size of 57 nm

After the ablation, some pictures were taken in order to record the as prepared solution. It is clear that the solution turns milky, which indicates that in fact there was ablation and nanoparticles are suspended in the solution. Also, to prove that in fact there were ablated species, the solution was irradiated with a lower power laser beam and compared with water. *Figure 55* shows these results.



Figure 55 – Laser irradiation of (left) water solution and (right) $Gd_5Si_2Ge_2$ as prepared solution. The difference is clear, with more dispersion of the irradiating light in the as prepared solution.

Besides SEM analysis, an EDS analysis was performed in order to estimate the composition of the final nanoparticles. The results are presented in *Figure 56*. The proportion of the atomic species is practically the same, except for the Germanium atoms. Also, it can be seen that the counting of Oxygen is relatively low, which is a good result considering that rare earth elements are easily oxidized.

An overall comparison between femtosecond and nanosecond ablation of $Gd_5Si_2Ge_2$ was performed considering the time of laser incidence with the average size of the resulting nanoparticles presented in *Figure 57*. As can be noticed, for short pulses duration, the average particle size does not present significant changes with the time of ablation while for the ns pulses the particle diameter suffer a large reduction from 210 nm to 40 nm. As mentioned on Chapter 2, fs pulses duration is shorter than the characteristic time of thermal dissipation of the material and this might be the reason for the absence of shifts on the particles size [14], [34]. Distinctly, for ns pulses, the thermal interactions are more evident, and the particle size reduction can be a consequence of the sequential ablations of the larger products [7], [76]. These observations are very important for future production of $Gd_5(Si,Ge)_4$

nanostructures through PLAL and can be used to understand how to obtain larger amounts of material.

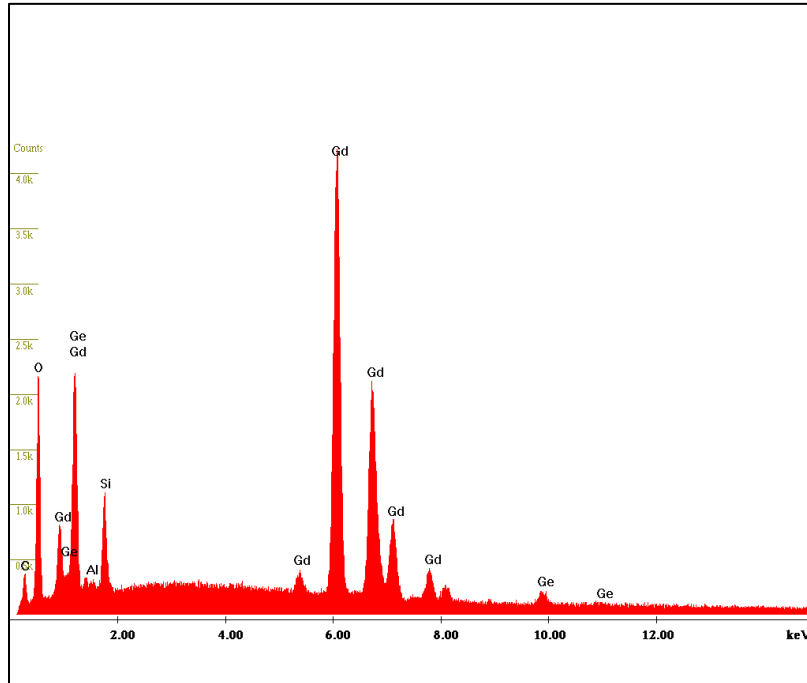


Figure 56 – EDS analysis of the $Gd_5Si_2Ge_2$ sample, after 8 hours of ablation.

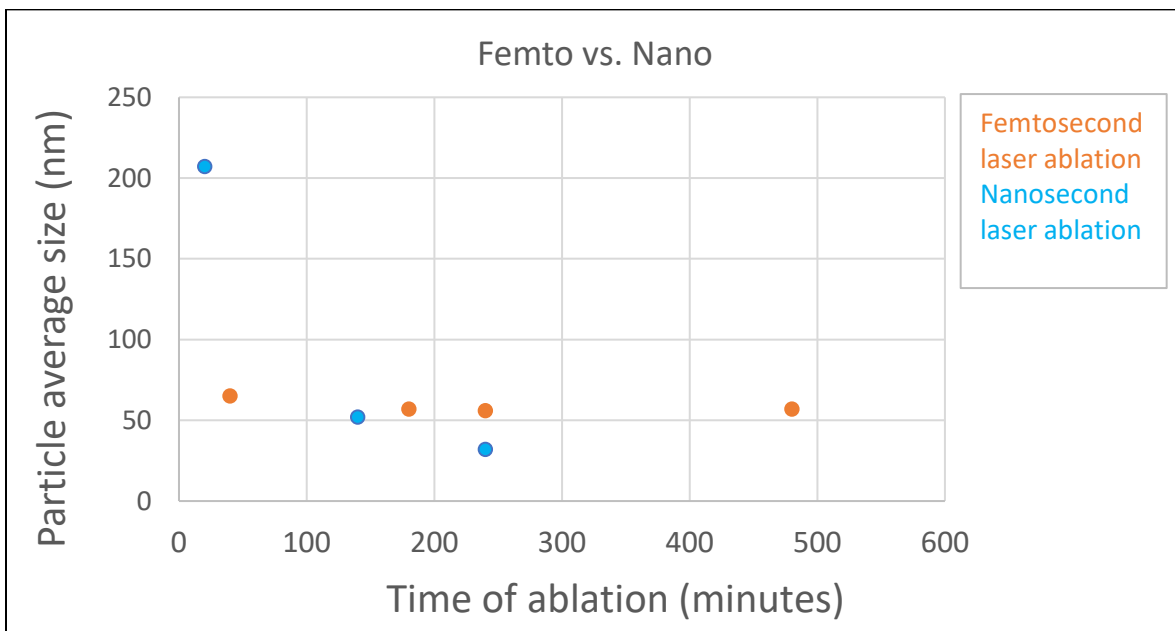


Figure 57 – Comparison between femtosecond and nanosecond on the average particle size depending on time of ablation.

Chapter 5 - Conclusions and Future Work

Given the results presented in this work, we can conclude that the production of $Gd_5(Si,Ge)_4$ nanoparticles using PLAL with femto- and nanoseconds pulsed lasers were successful. The study on the difference between each ablation method indicate that ultrashort lasers products present a more uniform size distribution than nanosecond ones. Besides that, we have also shown that longer ablation periods are desirable for acquiring larger amounts of samples. The SEM images indicate the presence of an organic matrix generated from the interactions between laser and target; however, to completely understand this formation process, transmission electronic microscopy (TEM) should be performed in the future. Additionally, XRD and magnetic measurements are also important for the confirmation of the NPs behavior. An initial attempt of measuring these samples were performed as shown below. However, due to the low amount of sample, there is a large contribution from the sample holder. Given this, we expect in the future to perform new measurements aiming to confirm the crystallographic and magnetic properties on the produced samples. Furthermore, the results are in large part in agreement with literature, and that means that this thesis was just a starting point for laser ablation in liquids in FIMUP and that this work will continue in the near future.

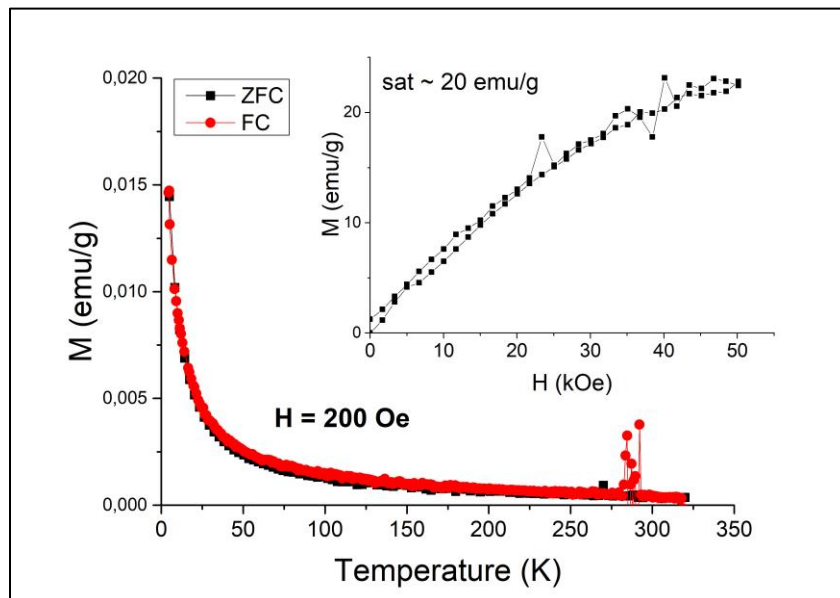


Figure 58 – $Gd_5Si_2Ge_2$ Magnetization dependence on temperature, for a fixed value of the magnetic field, for the cooling and heating curves, for a low amount of sample collected. The resulting saturation magnetization is very low comparing to previous results

Bibliography

- [1] V. K. Pecharsky and K. A. Gschneidner, Jr., "Giant Magnetocaloric Effect in $Gd_5Si_2Ge_2$," *Phys. Rev. Lett.*, vol. 78, no. 23, pp. 4494–4497, 1997.
- [2] V. Andrade, "The effect of nanostructuring on the Magnetostrictive and Magnetocaloric effect of the $R_5(Si, Ge)_4$ alloys 1 The Magnetostrictive Effect (MS)," vol. 5, pp. 1–24, 2016.
- [3] J. H. Belo, "Nanostructuring $Gd_5(Si,Ge)_4$ multifunctional materials," Faculty of Sciences of the University of Porto, 2017.
- [4] F. H. Belo and A. Faculdade, "Materials : Phase-Controlled Synthesis and Atomic Studies," vol. 5, 2010.
- [5] W. Choe, V. K. Pecharsky, A. O. Pecharsky, K. A. Gschneidner, V. G. Young, and G. J. Miller, "Making and Breaking Covalent Bonds across the Magnetic Transition in the Giant Magnetocaloric Material $Gd_5Si_2Ge_2$," vol. 827, no. 3, pp. 4617–4620, 2000.
- [6] A. L. Pires *et al.*, "Phase competitions behind the giant magnetic entropy variation: $Gd_5Si_2Ge_2$ and $Tb_5Si_2Ge_2$ case studies," *Entropy*, vol. 16, no. 7, pp. 3813–3831, 2014.
- [7] G. W. Yang, "Laser ablation in liquids: Applications in the synthesis of nanocrystals," *Prog. Mater. Sci.*, vol. 52, no. 4, pp. 648–698, 2007.
- [8] L. Mohammed, H. G. Gomaa, D. Ragab, and J. Zhu, "Magnetic nanoparticles for environmental and biomedical applications: A review," *Particuology*, vol. 30, pp. 1–14, 2017.
- [9] P. Liu, H. Cui, C. X. Wang, and G. W. Yang, "From nanocrystal synthesis to functional nanostructure fabrication: Laser ablation in liquid," *Phys. Chem. Chem. Phys.*, vol. 12, no. 16, pp. 3942–3952, 2010.
- [10] J. Xiao, P. Liu, C. X. Wang, and G. W. Yang, "External field-assisted laser ablation in liquid: An efficient strategy for nanocrystal synthesis and nanostructure assembly," *Prog. Mater. Sci.*, vol. 87, pp. 140–220, 2017.
- [11] S. B. Ogale, P. P. Patil, D. M. Phase, S. A. Kulkarni, S. V. Ghaisas, and V. G. Bhide, "Reactive Quenching At Liquid-Solid Interface Induced By Pulsed Ruby Laser Treatment: Aqueous Oxidation of Iron.," *Mater. Res. Soc. Symp. Proc.*, vol. 74, no. 3, pp. 4–7, 1987.
- [12] J. P. Sylvestre, A. V. Kabashin, E. Sacher, and M. Meunier, "Femtosecond laser ablation of

- gold in water: Influence of the laser-produced plasma on the nanoparticle size distribution,” *Appl. Phys. A Mater. Sci. Process.*, vol. 80, no. 4, pp. 753–758, 2005.
- [13] S. B. Ogale, “215 pulsed-laser-induced and ion-beam-induced surface synthesis and modification of oxides , nitrides and carbides*,” vol. 163, 1988.
- [14] D. Tan, S. Zhou, J. Qiu, and N. Khusro, “Preparation of functional nanomaterials with femtosecond laser ablation in solution,” *J. Photochem. Photobiol. C Photochem. Rev.*, vol. 17, pp. 50–68, 2013.
- [15] D. Perez and L. J. Lewis, “Molecular-dynamics study of ablation of solids under femtosecond laser pulses,” *Phys. Rev. B - Condens. Matter Mater. Phys.*, vol. 67, no. 18, pp. 1–15, 2003.
- [16] A. Miotello and R. Kelly, “Critical assessment of thermal models for laser sputtering at high fluences,” *Appl. Phys. Lett.*, vol. 67, p. 3535, 1995.
- [17] D. Puerto *et al.*, “Imaging of plasma formation, ablation and phase explosion upon femtosecond laser irradiation of crystalline Si and Ge,” *CLEO/Europe - EQEC 2009 - Eur. Conf. Lasers Electro-Optics Eur. Quantum Electron. Conf.*, vol. 14186, no. 1995, p. 225502, 2009.
- [18] L. Ayers, “Spinodal Decomposition The Mechanism of Spinodal Decomposition,” vol. 2, no. 1, pp. 1–10, 2012.
- [19] C. Cheng and X. Xu, “Mechanisms of decomposition of metal during femtosecond laser ablation,” *Phys. Rev. B - Condens. Matter Mater. Phys.*, vol. 72, no. 16, pp. 1–15, 2005.
- [20] B. Wu and Y. C. Shin, “A simple model for high fluence ultra-short pulsed laser metal ablation,” *Appl. Surf. Sci.*, vol. 253, no. 8, pp. 4079–4084, 2007.
- [21] D. Perez and L. J. Lewis, “Ablation of Solids under Femtosecond Laser Pulses,” *Phys. Rev. Lett.*, vol. 89, no. 25, pp. 1–4, 2002.
- [22] P. Lorazo, L. J. Lewis, and M. Meunier, “Thermodynamic pathways to melting, ablation, and solidification in absorbing solids under pulsed laser irradiation,” *Phys. Rev. B - Condens. Matter Mater. Phys.*, vol. 73, no. 13, pp. 1–22, 2006.
- [23] B. N. Chichkov, C. Momma, S. Nolte, F. Von Alvensleben, and A. Tünnermann, “Femtosecond, picosecond and nanosecond laser ablation of solids,” *Appl. Phys. A Mater. Sci. Process.*, vol. 63, no. 2, pp. 109–115, 1996.
- [24] S. S. Harilal, J. R. Freeman, P. K. Diwakar, and A. Hassanein, “Laser-Induced Breakdown Spectroscopy,” vol. 182, 2014.

- [25] J. Perrière, C. Boulmer-Leborgne, R. Benzerga, and S. Tricot, "Nanoparticle formation by femtosecond laser ablation," *J. Phys. D. Appl. Phys.*, vol. 40, no. 22, pp. 7069–7076, 2007.
- [26] J. König, S. Nolte, and A. Tünnermann, "Plasma evolution during metal ablation with ultrashort laser pulses.," *Opt. Express*, vol. 13, no. 26, pp. 10597–10607, 2005.
- [27] A. V. Kabashin and M. Meunier, "Synthesis of colloidal nanoparticles during femtosecond laser ablation of gold in water," *J. Appl. Phys.*, vol. 94, no. 12, pp. 7941–7943, 2003.
- [28] D. Werner and S. Hashimoto, "Improved working model for interpreting the excitation wavelength- and fluence-dependent response in pulsed laser-induced size reduction of aqueous gold nanoparticles," *J. Phys. Chem. C*, vol. 115, no. 12, pp. 5063–5072, 2011.
- [29] D. Werner, A. Furube, T. Okamoto, and S. Hashimoto, "Femtosecond laser-induced size reduction of aqueous gold nanoparticles: In situ and pump-probe spectroscopy investigations revealing coulomb explosion," *J. Phys. Chem. C*, vol. 115, no. 17, pp. 8503–8512, 2011.
- [30] A. Plech, V. Kotaidis, M. Lorenc, and J. Boneberg, "Femtosecond laser near-field ablation from gold nanoparticles," *Nat. Phys.*, vol. 2, no. 1, pp. 44–47, 2006.
- [31] A. Menéndez-Manjón and S. Barcikowski, "Hydrodynamic size distribution of gold nanoparticles controlled by repetition rate during pulsed laser ablation in water," *Appl. Surf. Sci.*, vol. 257, no. 9, pp. 4285–4290, 2011.
- [32] A. Santagata *et al.*, "Carbon-based nanostructures obtained in water by ultrashort laser pulses," *J. Phys. Chem. C*, vol. 115, no. 12, pp. 5160–5164, 2011.
- [33] D. Riabinina, M. Chaker, and J. Margot, "Dependence of gold nanoparticle production on pulse duration by laser ablation in liquid media," *Nanotechnology*, vol. 23, no. 13, 2012.
- [34] E. Akman, B. G. Oztoprak, M. Gunes, E. Kacar, and A. Demir, "Effect of femtosecond Ti:Sapphire laser wavelengths on plasmonic behaviour and size evolution of silver nanoparticles," *Photonics Nanostructures - Fundam. Appl.*, vol. 9, no. 3, pp. 276–286, 2011.
- [35] É. Boulais, R. Lachaine, and M. Meunier, "Plasma mediated off-resonance plasmonic enhanced ultrafast laser-induced nanocavitation," *Nano Lett.*, vol. 12, no. 9, pp. 4763–4769, 2012.
- [36] J. Wang, H. Niino, and A. Yabe, "One-step microfabrication of fused silica by laser ablation of an organic solution," *Appl. Phys. A Mater. Sci. Process.*, vol. 68, no. 1, pp. 111–113, 1999.
- [37] Y. Kawaguchi, X. Ding, A. Narazaki, T. Sato, and H. Niino, "Transient pressure induced by laser ablation of liquid toluene: toward the understanding of laser-induced backside wet etching,"

Appl. Phys. A, vol. 79, no. 4–6, pp. 883–885, 2004.

- [38] J. Singh, M. Vellaikal, and J. Narayan, “Laser-enhanced synthesis and processing of diamond films from liquid hydrocarbons,” *J. Appl. Phys.*, vol. 73, no. 9, pp. 4351–4356, 1993.
- [39] A. K. Sharma, H. G. Salunke, G. P. Das, P. Ayyub, and M. S. Multani, “Electronic structure of the 4H polytype of diamond,” *J. Phys. Condens. Matter*, vol. 8, no. 31, pp. 5801–5809, 1996.
- [40] V. A. Ermakov *et al.*, “Size Control of Silver-Core/Silica-Shell Nanoparticles Fabricated by Laser-Ablation-Assisted Chemical Reduction,” *Langmuir*, vol. 33, no. 9, pp. 2257–2262, 2017.
- [41] T. Sakka, K. Saito, and Y. H. Ogata, “Confinement effect of laser ablation plume in liquids probed by self-absorption of C2 Swan band emission,” *J. Appl. Phys.*, vol. 97, no. 1, 2005.
- [42] T. Sakka, H. Oguchi, and Y. H. Ogata, “Emission spectroscopy of ablation plumes in liquid for analytical purposes,” *J. Phys. Conf. Ser.*, vol. 59, no. 1, pp. 559–562, 2007.
- [43] L. Berthe, R. Fabbro, P. Peyre, L. TOLLIER, and E. Bartnicki, “Shock waves from a water-confined laser-generated plasma,” *J. Appl. Phys.*, vol. 82, no. 6, pp. 2826–2832, 1997.
- [44] S. Zhu, Y. F. Lu, and M. H. Hong, “Laser ablation of solid substrates in a water-confined environment,” *Appl. Phys. Lett.*, vol. 79, no. 9, pp. 1396–1398, 2001.
- [45] S. Zhu, Y. F. Lu, M. H. Hong, and X. Y. Chen, “Laser ablation of solid substrates in water and ambient air,” *J. Appl. Phys.*, vol. 89, no. 4, pp. 2400–2403, 2001.
- [46] G.-W. Yang, J.-B. Wang, and Q.-X. Liu, “Preparation of nano-crystalline diamonds using pulsed laser induced reactive quenching,” *J. Phys. Condens. Matter*, vol. 10, no. 35, pp. 7923–7927, 1999.
- [47] C. X. Wang and G. W. Yang, “Thermodynamics of metastable phase nucleation at the nanoscale,” *Mater. Sci. Eng. R Reports*, vol. 49, no. 6, pp. 157–202, 2005.
- [48] C. X. Wang, P. Liu, H. Cui, and G. W. Yang, “Nucleation and growth kinetics of nanocrystals formed upon pulsed-laser ablation in liquid,” *Appl. Phys. Lett.*, vol. 87, no. 20, pp. 1–3, 2005.
- [49] B. Verhoff, S. S. Harilal, J. R. Freeman, P. K. Diwakar, and A. Hassanein, “Dynamics of femto- and nanosecond laser ablation plumes investigated using optical emission spectroscopy,” *J. Appl. Phys.*, vol. 112, no. 9, 2012.
- [50] S. H. Lin, A. A. Villaeys, and Y. Fujimura, “Advances in Multi-Photon Processes and Spectroscopy,” vol. 22, 2014.

- [51] L. V. Keldysh, "Ionization in the field of a strong electromagnetic wave," *Sov. Phys. JETP*, vol. 20, no. 5, pp. 1307–1314, 1965.
- [52] A. Kaiser and B. Rethfeld, "Microscopic processes in dielectrics under irradiation by subpicosecond laser pulses," *Phys. Rev. B - Condens. Matter Mater. Phys.*, vol. 61, no. 17, pp. 11437–11450, 2000.
- [53] V. Zorba, J. Syzdek, X. Mao, R. E. Russo, and R. Kostecki, "Ultrafast laser induced breakdown spectroscopy of electrode/electrolyte interfaces," *Appl. Phys. Lett.*, vol. 100, no. 23, 2012.
- [54] J. Lam, "Pulsed Laser Ablation in Liquid : towards the comprehension of the growth processes
 To cite this version : PULSED LASER ABLATION IN LIQUID ;," 2015.
- [55] N. Tarasenko, V. Pankov, A. Butsen, and N. Tarasenko, "Laser Assisted Synthesis, Structural and Magnetic Characterization of Gadolinium Germano-Silicide Nanoparticles in Liquid," *J. Nanosci. Nanotechnol.*, vol. 16, no. 7, pp. 7451–7460, 2016.
- [56] N. Tarasenko, A. Butsen, V. Pankov, and N. Tarasenko, "Structural defects and magnetic properties of gadolinium silicide nanoparticles synthesized by laser ablation technique in liquid," *Phys. Status Solidi Basic Res.*, vol. 250, no. 4, pp. 809–814, 2013.
- [57] A. Butsen, N. Tarasenko, N. Tarasenko, and V. Pankov, "PREPARATION OF COMPOSITE NANOPARTICLES BY LASER PROCESSING OF THE MIXTURE OF COLLOIDAL SOLUTIONS," pp. 287–290, 2015.
- [58] I. Encyclopedia Britannica, "SEM Setup," 2008. [Online]. Available: <https://media1.britannica.com/eb-media/88/113688-004-B14FDB14.jpg>.
- [59] "electron interaction." [Online]. Available: https://en.wikipedia.org/wiki/Scanning_electron_microscope#/media/File:Electron_Interaction_with_Matter.svg.
- [60] O. L. Krivanek *et al.*, "Atom-by-atom structural and chemical analysis by annular dark-field electron microscopy," *Nature*, vol. 464, no. 7288, pp. 571–574, 2010.
- [61] "STEM setup." [Online]. Available: https://en.wikipedia.org/wiki/Scanning_transmission_electron_microscopy#/media/File:STEM_fig.tif.
- [62] "EDX scheme." [Online]. Available: https://en.wikipedia.org/wiki/Energy-dispersive_X-ray_spectroscopy#/media/File:EDX-scheme.svg.

- [63] N. D. M. Neil W. Ashcroft, *Solid State Physics - Ashcroft, Neil W, Mermin, David N.* 1976.
- [64] “Bragg law scheme.” [Online]. Available: https://www.google.com/search?tbm=isch&q=braggs+law&chips=q:braggs+law,online_chips:bragg+scattering&sa=X&ved=0ahUKEwit49zJwaXeAhVLDsAKHWIFABIQ4IYIKSgB&biw=1366&bih=626&dpr=1#imgrc=ALE0PSOMs5-lnM:
- [65] “Bragg Brentano Geometry.” [Online]. Available: https://www.google.com/search?q=bragg+brentano+geometry+xrd&source=lnms&tbm=isch&sa=X&ved=0ahUKEwipqJ2jnqzcAhUPr6QKHQ-xCHYQ_AUICigB&biw=1366&bih=635#imgdii=OGQms8zdlz1ENM:&imgrc=IF5JQyi0hnTG3M:
- [66] “Parallel beam geometry.” [Online]. Available: https://www.google.com/search?biw=1366&bih=586&tbm=isch&sa=1&ei=0RNRW76IPMX8kwXsgYKwCw&q=xrd+setup&oq=xrd+setup&gs_l=img.3..35i39k1.792598.794128.0.794366.9.8.0.0.0.0.232.452.2-2.2.0....0...1c.1.64.img..7.2.450...0j0i67k1.0.KUr1LUuECrw#imgrc=4ahDtTIAyKHxv.
- [67] “VSM scheme.” [Online]. Available: https://www.google.pt/search?biw=1366&bih=626&tbm=isch&sa=1&ei=2JjZW7qEFleOlwSLkrDgCw&q=vibrating+sample+magnetometer&oq=Vibrat&gs_l=img.3.0.35i39k1j0i4j0i30k1i5.1928.3400.0.4390.7.7.0.0.0.0.137.592.1j4.5.0....0...1c.1.64.img..2.5.590...0i67k1.0.9pHjQrv3.
- [68] J. H. Belo *et al.*, “Phase control studies in $Gd_5Si_2Ge_2$ giant magnetocaloric compound,” *J. Alloys Compd.*, vol. 529, pp. 89–95, 2012.
- [69] L. To, T. H. E. Editor, and G. H. Rao, “Correlation between crystal structure and magnetic properties,” vol. 12, pp. 93–99, 2000.
- [70] V. K. Pecharsky and K. A. Gschneidner, “Tunable magnetic regenerator alloys with a giant magnetocaloric effect for magnetic refrigeration from ~20 to ~290 K,” *Appl. Phys. Lett.*, vol. 70, no. 24, pp. 3299–3301, 1997.
- [71] C. Floss, C. Le Guillou, and A. Brearley, “Coordinated NanoSIMS and FIB-TEM analyses of organic matter and associated matrix materials in CR3 chondrites,” *Geochim. Cosmochim. Acta*, vol. 139, pp. 1–25, 2014.
- [72] N. R. Checca, R. J. Caraballo-Vivas, R. Torrão, A. Rossi, and M. S. Reis, “Phase composition and growth mechanisms of half-metal Heusler alloy produced by Pulsed Laser Deposition:

From core-shell nanoparticles to amorphous randomic clusters,” *Mater. Chem. Phys.*, vol. 196, pp. 103–108, 2017.

- [73] D. Muñetón Arboleda *et al.*, “Synthesis of Ni Nanoparticles by Femtosecond Laser Ablation in Liquids: Structure and Sizing,” *J. Phys. Chem. C*, vol. 119, no. 23, pp. 13184–13193, 2015.
- [74] D. M. Arboleda *et al.*, “Structure , configuration and sizing of Ni nanoparticles generated by ultrafast laser ablation in different media,” vol. 9547, pp. 1–9, 2015.
- [75] D. A. Links, “Novel issues of morphology , size , and structure of Pt nanoparticles in chemical engineering : surface attachment , aggregation or agglomeration ,” pp. 1320–1334, 2012.
- [76] E. Messina, “Thesis_Metal Nanoparticles Produced by Pulsed Laser Ablation in Liquid Environment,” 2010.